A Preliminary Study of the Effect of the Chirped Rotating Wall on a Positron Cloud

Phillip John

Supervisor: Professor Stefan J. Eriksson

A thesis submitted in fulfilment of the requirements for the degree of Master of Philosophy

Swansea University
Prifysgol Abertawe

Department of Physics, College of Science

Swansea University

June 8, 2023

Abstract

The density of the positron cloud is a crucial parameter in many applications of accumulated positrons. Previous work has shown that adjusting the frequency of the rotating wall potential following positron accumulation can be used to control the density of positron clouds. In this work, positron clouds were studied after being compressed using a linear rotating wall frequency sweep under a selection of rotating wall drive amplitudes and cooling gas pressures following an initial static frequency compression. This was performed for SF_6, CF_4, and briefly for CO. The effect of changing the cooling gas appears congruent to that shown by the static frequency case. The results are in qualitative agreement with previous work by Deller *et al.*, and compare briefly but favourably to a simplistic numerical model.

Declaration

This work has not previously been accepted in substance for any degree and is not being concurrently submitted in candidature for any degree.

Phillip Thomas John
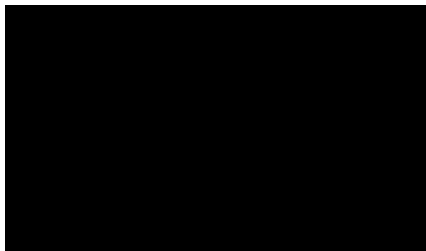Swansea, June 8, 2023
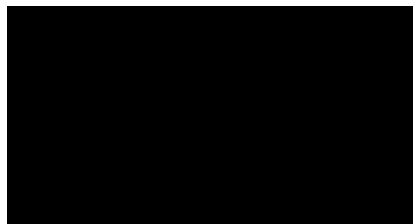
This thesis is the result of my own investigations, except where otherwise stated. Other sources are acknowledged by footnotes giving explicit references. A bibliography is appended.
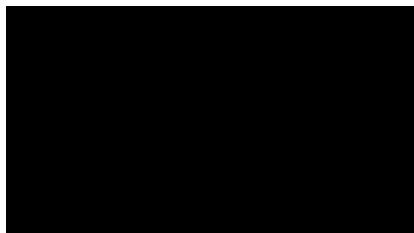
Phillip Thomas John
Swansea, June 8, 2023
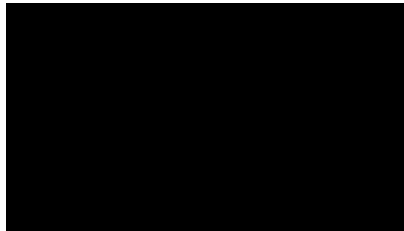
I hereby give consent for my thesis, if accepted, to be available for photocopying and for inter-library loan, and for the title and summary to be made available to outside organisations.

Phillip Thomas John
Swansea, June 8, 2023

The University's ethical procedures have been followed and, where appropriate, that ethical approval has been granted.

Phillip Thomas John
Swansea, June 8, 2023

Acknowledgements

Contents

List of Figures

Chapter 1

Introduction

1.1 The Positron

1.1.1 Historical Context

In 1898, German-born British physicist Arthur Schuster sent a pair of letters to the scientific journal *Nature* [1] in which he whimsically hypothesised the existence of anti-atoms. Whilst purely speculative, it was in these texts that the term *antimatter* was coined.

It was not until 1928, when Paul Dirac published his quantum theory of the electron, that the modern theory of antimatter truly began. In this seminal work, Dirac postulated his relativistically invariant wave equation which implied that both positive and negative energy solutions could exist for the electron [2].

Initially puzzled by the unavoidable physical consequences that his model seemed to suggest, Dirac would later publish another paper in 1931 in which he postulated that the "anti-electron" would have an opposite charge and identical mass to that of the electron [3], and that it would annihilate with its positively-charged counterpart; the particle was later termed the *positron* in Carl Anderson's discovery paper in 1933, for which, Anderson was awarded the 1936 Nobel Prize for Physics [4]. Despite concurrent discovery by Blackett and Occhialini [5], Anderson published first, and his experiment produced one of the best known, and widely referenced images in positron physics to date, shown in figure 1.1. The experiment consisted of a sealed vertical Wilson cloud chamber, filled with a supersaturated vapour, surrounded by
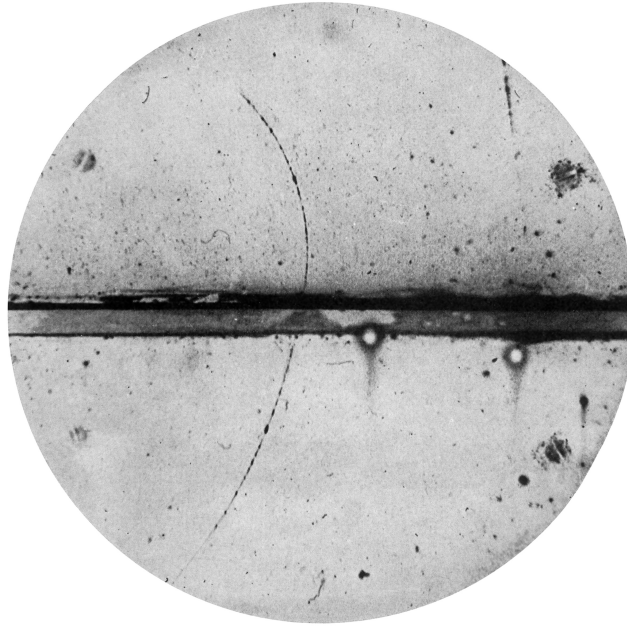
Figure 1.1: The cloud chamber photograph of the first positron identified. The trail of a 63 MeV positron passing through the 6 mm lead plate is visible, emerging as a 23 MeV positron [4].

a magnetic field of ∼15,000 G to deflect charged particles via the Lorentz force. Cosmic rays passed through this chamber, creating paths of ionised gas molecules. In such a chamber, these ions act as condensation nuclei that condense droplets from the vapour into mist-like trails which can be imaged. Anderson's cloud chamber also contained a 6 mm lead plate which acted as an energy degrader for charge comparisons with electrons. Since the incident particle deflected in the opposite direction to the electron within the magnetic field, and after comparing the particle's energy loss through the plate with the measured mean for that of electrons, Anderson determined that the particle was positively charged and that its charge 'is less than twice, and is probably exactly equal to, that of the proton'. Furthermore, the length of the track emerging from the plate in the image was determined to be at least ten times greater than what would have been possible for a proton with the same curvature. Anderson was thereby able to place an upper limit on the mass of the positron of approximately 20 times the electron mass.

1.1.2 Positron Emission

Pair Production & Radioisotopes

As the generation of greater numbers of positrons became requisite for experimental advancement, a means to produce positrons artificially was established: pair production. Pair production is the phenomenon observed by Blackett and Occhialini during their Geiger counter-triggered images of a cloud chamber that showed two separate particles clearly spiralling in opposite directions from a common origin. What had been observed in the images was the result of a cosmic ray of an energy greater than the sum of the rest mass energies of the particles that were produced, approaching an atomic nucleus. In the case of an electron-positron pair, this would need to be at least $1.022\,\text{MeV}$. This energy requirement is easily met in nuclear reactor settings and particle accelerator facilities; massive positron pulses have been achieved by smaller, dedicated linear accelerators (LINAC) that implant $180\,\text{MeV}$ electrons into a high-Z target i.e., of high atomic number, usually a dense metal, to produce a slow positron beam upon energy moderation. Most recently, this has been achieved by the GBAR experiment (Gravitational Behaviour of Antihydrogen at Rest) with a $9\,\text{MeV}$ electron beam, producing on the order of 10^{10} positrons for use in dense positronium cloud formation. [6] As the electrons' motion is impeded by the medium's nuclei, they release *bremsstrahlung*, literally "braking radiation" that will generate positrons directly via pair production [7], the excess photon energy being transferred into the fermions' motion with an average transferred to each of

$$< E_k >= \frac{1}{2}(\hbar\nu - 2m_ec^2) \tag{1.1}$$

assuming nuclear recoil is negligible.

There are obvious, costly caveats to producing low-energy positrons in this manner. Alternatively, many experimental applications and studies where such high yield is not necessary require lower-energy positron beams to be manipulated, as is featured in this work, that benefit from a more conservative low-energy positron generation procedure.

In 1934, the daughter of Marie Curie, Irène, and her husband Frédéric, observed the first recorded instance of β^+ decay, the process by which isotopes emit a positron [8]. There are numerous radioisotopes (see table 1.1), both artificial and naturally occurring, that are known for emitting positrons via this weak nuclear decay process, with half-lives ranging from minutes to hours such as ^{11}C, ^{64}Cu, ^{13}N, and ^{55}Co which are used primarily in positron emission tomography, and those with half-lives better suited to laboratory use such as ^{26}Al, ^{22}Na, and ^{40}K. As mentioned previously, whilst pair production methods can produce large numbers of positrons, this is not necessary, or practical in a compact laboratory setting where lower yield experimental requirements do not mandate long linear accelerators and cumbersome biological shielding. As such, most laboratory positron sources are radioisotope-based.

Table 1.1: A selection of radioisotopes & their properties, known for their use in generating low-energy e$^+$ beams [9].

Isotope	β^+ Branching ratio	Endpoint energy (MeV)	Half-life	Typical production mechanism
^{22}Na	0.91	0.54	2.6 yr	^{24}Mg(d,α)
^{58}Co	0.15	0.47	70.8 d	^{58}Ni(n,p)
^{64}Cu	0.19	0.65	12.7 hr	^{63}Cu(n,γ)
^{11}C	0.99	0.96	20.4 min	^{11}B(p,n)

Sodium-22

Many of the aforementioned isotopes have been used to generate low-energy positron beams as seen in [10, 11] but, of particular efficacy and conventional usage today is the sodium radioisotope ^{22}Na. This artificially produced radioisotope has a half-life of 2.6 years making it reasonably well-suited to laboratory use. It has a β^+ branching ratio of $\sim$90% with the remainder mostly made up of electron capture transitions (9.6%) [12] and can be produced with activities on the order of 10^9 Bq. The radioisotope is also appealing due to a by-product of its decay scheme; ^{22}Na predominantly decays to a very short lived (3.7 ps) excited state of ^{22}Ne (equation 1.2) which in turn releases a characteristic gamma ray photon with energy 1.274 MeV.

The emitted positrons will have an energy ranging from $0 - 546$ keV [12].

$$^{22}_{11}\text{Na} \xrightarrow{\text{t}_{\frac{1}{2}}=2.6 \text{ yr}} {}^{22}_{10}\text{Ne}^* + e^+ + \nu_e$$
$$\hookrightarrow {}^{22}_{10}\text{Ne} + \gamma_{(3.7\,ps)}$$

(1.2)
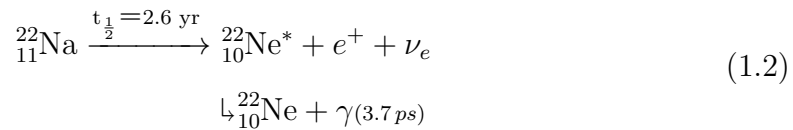
This 'trigger' photon has found use as the *start* signal when conducting positron annihilation lifetime measurements [9, 13].

1.1.3 Positron Moderation

What follows is a concise description of the physics of moderation and its experimental milestones that have led this innovation to the current status of compact, near-monoenergetic, low-energy positron beams in use, including the one featured in this work.

Brief Physical Context

Despite the popularity of radioisotope-based slow positron beams created through β^+-decay, there are some disadvantages. Whilst the reduction in beam intensity over time due to the source half-life is manageable for ^{22}Na, the broad kinetic energy distribution of the emitted positrons, a graphical example of which can be seen in figure 1.2, makes them unsuitable for most experimental applications. As such, considerable efforts have been directed toward producing high-yield, low-energy positron beams with as narrow an energy spread as possible. When energetic positrons interact with a solid they will rapidly lose energy via a number of processes, the three to note in order of descending energy threshold are inelastic collisions with core and conduction electrons, plasmon excitation at the 10s of eV range, and phonon scattering at eV energies. The precise energy loss mechanism will be dependent on the nature of the bulk material onto which the positrons impinge.

In metals, positrons on the order of keV can rapidly drop to very low energies i.e., thermalise, in picoseconds [14]. A positron that thermalises within a single *average diffusion length*, L_+, of the surface, defined as the average distance a thermalised positron travels before annihilation, is able to diffuse back to the surface. Once a thermalised positron reaches the material surface boundary it can then most likely
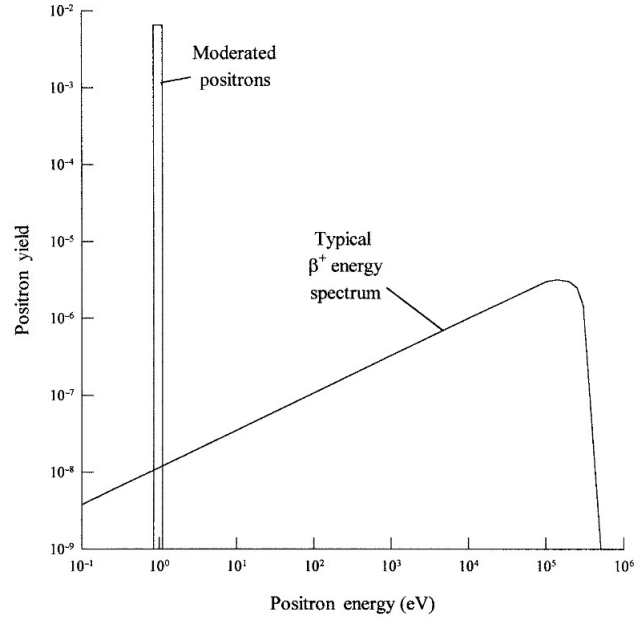
Figure 1.2: A comparison of the energy distribution of moderated & unmoderated positrons [9].

partake in one of three events: it can fall into a nearby surface well and annihilate there, it can acquire an electron and proceed to annihilate as positronium, or the preferred scenario; it can leave the surface and be emitted into vacuum as a moderated, low-energy positron. More specifically, the energy of the released positron will be determined primarily by the positron *work function*, ϕ_+ of the surface, provided that it's negative, except in the case of a *rare gas solid* (RGS) in which the positrons with energies exceeding the work function can be emitted [15]. The positron work function in this instance being the minimum amount of work required to liberate a positron from the bulk material,

$$-\phi_+ = \mu_+ + D \tag{1.3}$$

where μ_+ is the chemical potential in the bulk and D is the surface dipole potential. The likelihood that the thermalised positron at the surface proceeds to the preferable scenario of emission into the vacuum is increased as ϕ_+ becomes more negative. The fraction of positrons that are able to thermalise and diffuse back to the surface is increased if the material has minimal inhomogeneities i.e., non-equilibrium defects that act as positron trapping centres which reduce the positrons' diffusion length. A more in-depth derivation of the following can be found in [9, 14, 15].

Experimental Advances

The first, albeit accidental and never journal-published experimental evidence of positron moderation, came in 1958 in the doctoral thesis of W.H. Cherry [10]. In this work, the moderator material used was chromium-on-mica and reduced the energy distribution of the remitted positrons with an measured efficiency of $\epsilon = 10^{-8}$. The first official journal publication of moderation came in 1969 when J. M. Madey implanted positrons into an aluminium coated polyethylene material narrowing the energy distribution to a peak of 20 eV [16]. Another breakthrough came in 1972 with the study by Canter *et al.*, who achieved an efficiency of $\epsilon = 3 \times 10^{-5}$ using a 'smoked' MgO powder coating on gold blades [17]. 1979 saw the first ultra-high vacuum (UHV) moderator made from a piece of single-crystal copper [18], producing an efficiency of 10^{-3} and in 1983, a metallic moderator that is used today was introduced: tungsten, its large positron work function made it an excellent moderator and its high melting point ensures that it can be easily annealed [19].

As of today, the most efficient moderator materials are classed as metallic, or RGS. There are advantages and disadvantages for both and therefore moderator-type is usually selected based on the experimental requirements. For example, RGS moderators like argon and neon, as is used in this work (see section 3.2.3), tend to produce higher efficiencies (as high as 1% [20]) than metallic moderators but also produce a broader energy spread due to lack of initial control over surface defects, tend to be more costly due to the required cryogenics and gas supply, and their performance degrades over time, whereas the highest quality metallic moderators are easier to maintain and affect a narrower energy spread, but yield a lower number of low-energy positrons.

1.2   Motivation & Thesis Outline

Compression of a positron cloud into as small and high-density a cloud as possible is of intrinsic value, not just for studying the collective behaviour of positrons in both the single-particle and plasma regimes, but also in the interest of maximising production of positronium for compact systems that use radioactive sources to produce low-energy positron beams. Positronium (Ps), the quasi-stable bound state of

an electron and a positron is currently being investigated and indeed used, as an ingredient in the production and study of antihydrogen via charge exchange reaction between Rydberg-Ps i.e., Ps in a highly-excited Rydberg state, and an antiproton [21, 22]. Or as in the case of the GBAR Experiment at CERN, interaction of a dense Ps cloud with antihydrogen to form a more easily manipulated antihydrogen-ion [6]. 'Rotating wall' compression, elucidated in sections 2.3, 2.4 and 3.2.5, has been used to compress positron clouds both in the independent particle regime and as non-neutral plasma.

It has been shown in previous work [23, 24] that adjusting the rotating wall frequency following accumulation i.e., chirping (with a 'static' rotating wall applied during the accumulation phase), can help to control the density of the accumulated cloud, but the literature is limited and further research is required.

This thesis aims to help characterise the behaviour of the rotating-wall-compressed positron cloud upon receiving further chirped compression in CF_4 gas under varying chirp and trap conditions, as well as SF_6 and CO. The results of the research are compared and contrasted to the only previous chirp-related work performed on the beamline [25], that which was performed with SF_6 as the cooling gas, thus drawing further conclusions on rotating wall chirp-enhanced compression and building an understanding of the effect of changing the cooling gas, as well as qualitative comparison to a simple toy model.

The thesis is structured as follows:

Chapter 2 will cover the physics and theoretical background of the relevant topics.

Chapter 3 presents a technological and contextual review of the beamline and its current status in Swansea.

Chapter 4 presents the experimental data & analyses.

Chapter 5 will conclude the thesis and discuss the potential for future work.

Chapter 2

Positron Manipulation: Theoretical Considerations

2.1 The Penning Trap

The Penning trap design was influenced by the Penning vacuum gauge that operates using a high voltage discharge in a magnetic field. The original Penning trap was designed and built by Hans Georg Dehmelt and Wolfgang Paul in the 1950s for which they were later jointly awarded the Nobel Prize in Physics in 1989 [26].

2.1.1 Lorentz Force

As this apparatus operates below the relativistic limit and is held under vacuum, the forces acting on a charged particle influenced by electric and magnetic fields, akin to a point charge, can be reasonably described in Cartesian coordinates by the equation,

$$\ddot{\mathbf{u}}(\mathbf{u}, \dot{\mathbf{u}}, t, q, m) = \frac{q}{m} \left[\mathbf{E(u,t)} + \dot{\mathbf{u}} \times \mathbf{B}(\mathbf{u}, t) \right] \tag{2.1}$$

where $\mathbf{u} = (x, y, z)$, q is elementary charge, m is particle mass and $\mathbf{E}$ & $\mathbf{B}$ are the electric and magnetic fields, respectively. A prefixal γ would denote the Lorentz factor which is taken as $\gamma \approx 1$ in the non-relativistic limit.

Equation (2.1) can be used, in conjunction with the appropriate potential that satisfies the Laplace condition to derive equations of motion for a charged particle in a Penning trap.

2.1.2   The Ideal Case

In 1842, English mathematician Samuel Earnshaw postulated in his work [27] a theorem that in accordance with Gauss' Law in free space, the divergence of an electric field derived from a potential is zero due to lack of charge density,

$$\nabla \cdot \mathbf{E} = \frac{\rho}{\varepsilon_0 \varepsilon_{\mathrm{r}}} = 0 \tag{2.2}$$

and as a consequence, no static electric field configuration can confine a test charge, or charged particle, in all three dimensions simultaneously i.e.,

$$\nabla^2 \phi = \nabla \cdot (\nabla \phi) = \nabla \cdot \mathbf{E} = 0 \tag{2.3}$$

This motivated the concept of ion trapping to find realisation with time-varying electric fields as in the Paul Trap [28] or, more relevant to this work, a static electric field superimposed with a strong, homogeneous magnetic field.

For three-dimensional confinement of charged particles, a potential energy minimum is required at a point in space to which corresponding forces will be directed from every direction. For the idealised case, we can seek a harmonic binding condition and use the relation,

$$\mathbf{F} = -\nabla U \tag{2.4}$$

where U is the potential energy. In Cartesian coordinates, a quadratic electrostatic potential can thus be stated as,

$$\phi(x, y, z) = \frac{\phi_0}{2d^2} \left(\alpha x^2 + \beta y^2 + \gamma z^2 \right) \tag{2.5}$$

where d is a trap geometry factor.

To satisfy the Laplace condition from equation (2.3), we see that $\alpha + \beta + \gamma = 0$. In the idealised Penning trap with rotational symmetry along the trap axis, z, we can set $\alpha = \beta = -1/2$ and $\gamma = 1$ and therefore the potential can be expressed as

$$\phi(x, y, z) = \frac{\phi_0}{2d^2} \left(z^2 - \frac{1}{2} \left(x^2 + y^2 \right) \right). \tag{2.6}$$
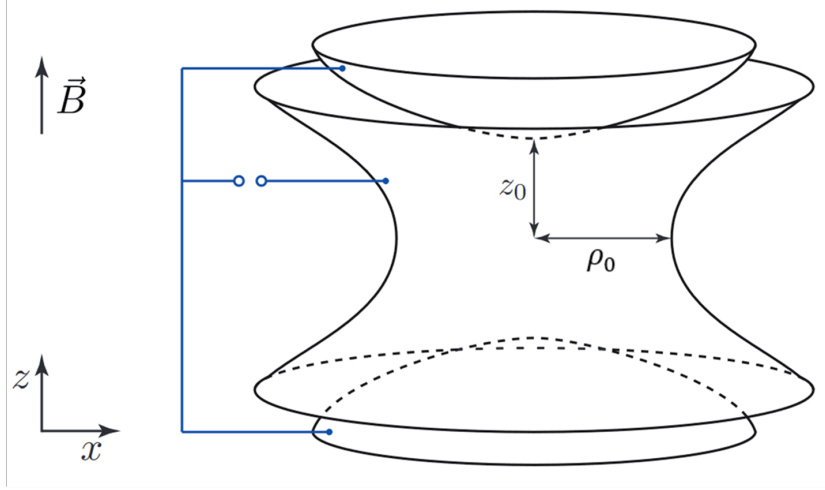
Figure 2.1: Schematic of an ideal Penning trap with hyperbolic electrodes designed by Dehmelt & Paul. There is a potential difference between the endcaps and the middle electrodes. The direction of the magnetic field is shown. Inspired by [29].

This potential describes the conventional 'ideal' design by Dehmelt and Paul that uses electrodes with hyperbolic inner surfaces, a diagram of which can be viewed in figure 2.1. This potential is realised by two idealised hyperbolic endcap electrodes and a corresponding ring electrode, generating a hyperbola of revolution around the trap axis. The endcap electrodes and ring electrode must adhere to the conditions,

$$z^2 = z_0^2 + \frac{\rho^2}{2} \tag{2.7a}$$

$$z^2 = \frac{\rho^2 - \rho_0^2}{2}, \tag{2.7b}$$

respectively, where z_0 and ρ_0 represent the shortest distance from the centre of the trap structure to the electrodes in the axial and radial directions as seen in figure 2.1.

Then the geometry factor d can be defined as

$$d = \sqrt{\frac{1}{2}\left(z_0^2 + \frac{\rho_0^2}{2}\right)} \tag{2.8}$$

One can determine the trapping frequencies and conditions by examining the equations of motion. By inserting the potential-derived expression for the electric field

and the axial magnetic field into equation (2.1), we arrive at

$$
m \begin{pmatrix} \ddot{x} \\ \ddot{y} \\ \ddot{z} \end{pmatrix} = \frac{q\phi_0}{2d^2} \begin{pmatrix} x \\ y \\ -2z \end{pmatrix} + q \begin{vmatrix} \hat{i} & \hat{j} & \hat{k} \\ \ddot{x} & \ddot{y} & \ddot{z} \\ 0 & 0 & B_z \end{vmatrix} \tag{2.9}
$$

which lead to the equations of motion:

$$
\ddot{x}(t) - \frac{q\phi_0}{2md^2}x(t) - \frac{q|\mathbf{B}|}{m}\dot{y}(t) = 0 \tag{2.10a}
$$

$$
\ddot{y}(t) - \frac{q\phi_0}{2md^2}y(t) + \frac{q|\mathbf{B}|}{m}\dot{x}(t) = 0 \tag{2.10b}
$$

$$
\ddot{z}(t) + \frac{q\phi_0}{md^2}z(t) = 0. \tag{2.10c}
$$

It is immediately apparent that the z-component is independent of the radial components and follows the form of an undamped harmonic oscillator with frequency,

$$
\omega_z = \sqrt{\frac{q\phi_0}{md^2}} \tag{2.11}
$$

called the *axial bounce frequency*. Since a free charged particle in an axial magnetic field exhibits a cyclotron motion in the radial plane according to equation (2.1), we can also define the *cyclotron frequency* as,

$$
\Omega = \frac{q|\mathbf{B}|}{m}. \tag{2.12}
$$

The motion in the transverse plane can be effectively described by introducing a complex variable function, $\Lambda(t) = x(t) + iy(t)$ to combine equations (2.10a) and (2.10b) thus,

$$
\ddot{\Lambda}(t) + i\Omega\dot{\Lambda}(t) - \frac{\omega_z^2}{2}\Lambda(t) = 0 \tag{2.13}
$$

By inserting a solution of the form $\Lambda(t) = e^{-i\omega t}$, we achieve a quadratic equation in ω:

$$
\omega^2 - \Omega\omega + \frac{\omega_z^2}{2} = 0. \tag{2.14}
$$

Solving this equation leads to a well-known expression including all relevant Penning trap eigenfrequencies:

$$\omega_\pm = \frac{1}{2}\left(\Omega \pm \sqrt{\Omega^2 - 2\omega_z^2}\right) \tag{2.15}$$

where ω_+ is the *modified* or *reduced* cyclotron frequency, named because under typical trapping parameters and requirements, is only slightly less than the cyclotron frequency, and ω_- (sometimes written ω_m) is the *magnetron frequency.*

Also under typical trapping conditions, $\Omega \gg \omega_z$, therefore a 1$^{\text{st}}$ order Taylor expansion can be performed on equation (2.15) to simplify expressions for ω_+ and ω_- thus:

$$\omega_- \approx \frac{\omega_z^2}{2\Omega} \tag{2.16a}$$

$$\omega_+ \approx \Omega - \omega_-. \tag{2.16b}$$

Finally, the confinement condition (or stability limit) i.e., stable trajectories, is met when the frequencies are real, as is evident by the discriminant of equation (2.15), i.e.,

$$\Omega > \sqrt{2}\omega_z \tag{2.17}$$

or equivalently,

$$B > \sqrt{\frac{2m\phi_0}{qd^2}}. \tag{2.18}$$

This shows that if the voltage between the electrodes, ϕ_0, is too great, the magnetic field can no longer radially confine particles. Typically, the eigenfrequency hierarchy,

$$\omega_- \gg \omega_z \gg \omega_+ < \Omega \tag{2.19}$$

exists. All three ideal Penning trap motions can be viewed superimposed in figure 2.2.
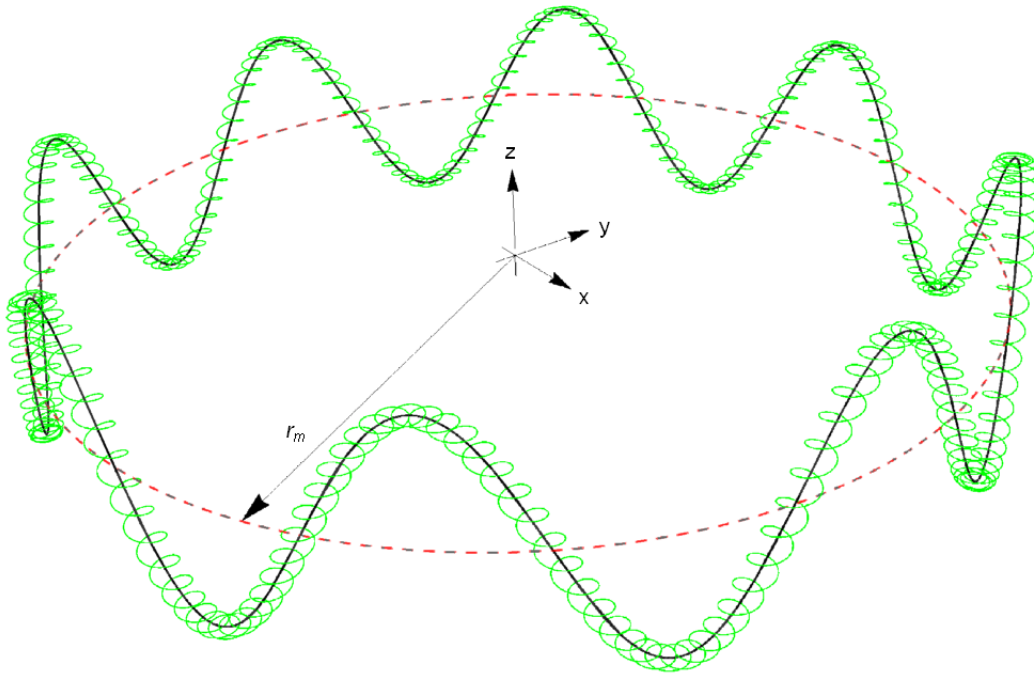
Figure 2.2: A plot showing a superposition of the three primary Penning trap motions. A particle (green) will follow the path of an epicycloid in the radial plane and a periodic motion along the trap axis. The green line represents the cyclotron motion, the black solid line represents axial bounce motion, and the dashed red line shows the magnetron orbit with radius r_{m}. From [23], pp.33.

2.1.3 Real-World Considerations

The previous discussion expects ideal, perfect conditions. In reality, the eigenfrequencies expressed in equation (2.15) are shifted due to imperfections in the cylindrically symmetric electric field and inhomogeneities in the cylindrically symmetric magnetic field. These can be more effectively characterised in cumbersome multipole series expansions that will not be discussed here; detail on how perturbations lead to complications can be found in [30].

Non-ideal deviations will also arise from potential ellipticity of the radial electric field components and other field misalignments between the electric field generated by the electrodes and the magnetic field. Finally, particle-particle interactions and the presence of image charges in the trap electrodes will distort from ideal conditions. These image charges will act to pull the charged species away from the trap centre while the space charge from interacting particles can lead to erratic frequency shifts and coupling (energy exchange) between the eigenfrequency modes. It's for this reason that the highest precision traps are typically designed to operate with single ions. All real-world Penning-type traps suffer from these deviations including the ones detailed below.

2.1.4   The Cylindrical/Penning-Malmberg Trap

The physical requirements of the ideal Penning trap originally designed by Dehmelt led to some practical disadvantages namely, perfectly hyperbolic electrodes are difficult to accurately manufacture and possess no opening through which to efficiently load ions/charged particles into the trap. A common variant of the Penning trap employed on a beamline apparatus is the Penning-Malmberg trap. It was recognised at an early stage that any rotationally symmetric electrode geometry is capable of generating a potential minimum along one axis and a maximum along the other i.e., a saddle point and that the potential in the vicinity of this point is a good approximation to a pure quadrupole potential. Thus, to provide simple coaxial particle loading, traversal, and ejection, the Penning-Malmberg trap replaces hyperbolic endcaps and a ring electrode with cylindrical electrodes, a three electrode case of which is visualised in figure 2.3.

This type of trap is used extensively for beamline apparatus due to its scalability, allowing for the application of asymmetric well configurations to trap charged species and accumulate positrons. The electric potential produced by this configuration is non-trivial and for brevity will not be derived here (see [31]) but an analytical expression for the three electrode structure with closed endcaps (L will only negligibly affect the solution provided the endcap electrodes are of comparable length to the centre electrode, thus the expression can be reasonably applied to open-end structures) can be calculated by solving the Laplace equation (equation (2.3)) in
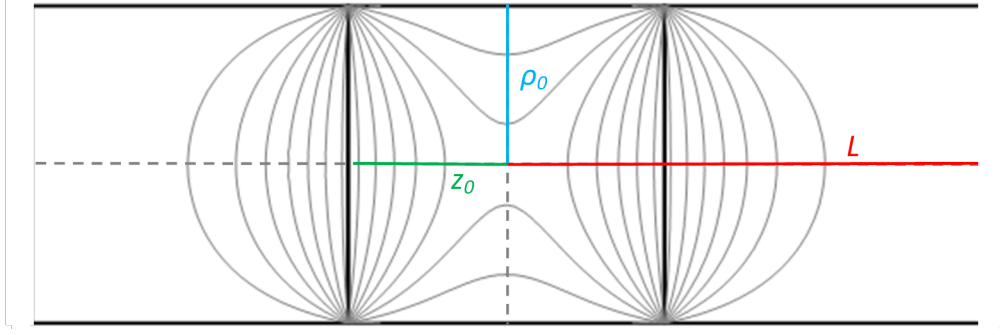
Figure 2.3: A 2D diagram of a cylindrical Penning-Malmberg trap with a single ring electrode (centre) and endcaps. The equipotential lines of the approximately quadratic electric field are visible, modelled by equation (2.20). Here, L is the axial trap length from the centre to the endcap/electrode end, z_0 is the ring electrode centre-to-edge length, and ρ_0 is the electrodes' inner radius.

cylindrical coordinates, yielding,

$$\phi(\rho, z) = \frac{2\phi_0}{L} \sum_{n=0}^{\infty} \frac{\sin(k_n z_0)}{k_n I_0(k_n \rho_0)} I_0(k_n \rho) \cos(k_n z) \qquad (2.20)$$

where $I_n(x)$ is a modified Bessel function of the 1$^\text{st}$ kind and k_n is defined as,

$$k_n = \frac{\pi}{L} \left(n + \frac{1}{2} \right) \qquad (2.21)$$

to ensure that the potential is zero at the endcap boundaries.

This potential brings forth a consequence that influences the investigations in this work: the fact that the axial bounce frequency, ω_z is dependent on both the parallel energy and the magnetron orbit radius of the positrons in the cloud. The axial bounce frequency is extracted via sinusoidal fit to data acquired from a '*magnetron kick*', detailed in section 3.2.5. This is showcased in figure 2.4. A variation of the Penning-Malmberg trap that is central to positron manipulation and indeed this work is the *buffer gas trap*, detailed below.

2.2 The Buffer Gas Trap

The buffer gas trap was developed in the mid-1980s by C. M. Surko, *et al.* [32] as a means of studying magnetically-confined fusion plasmas i.e., tokamak plasmas, specifically to mitigate the rapid transport of charged electron-mass particles for the purposes of storage between tokamak discharge cycles. Informally called the Surko
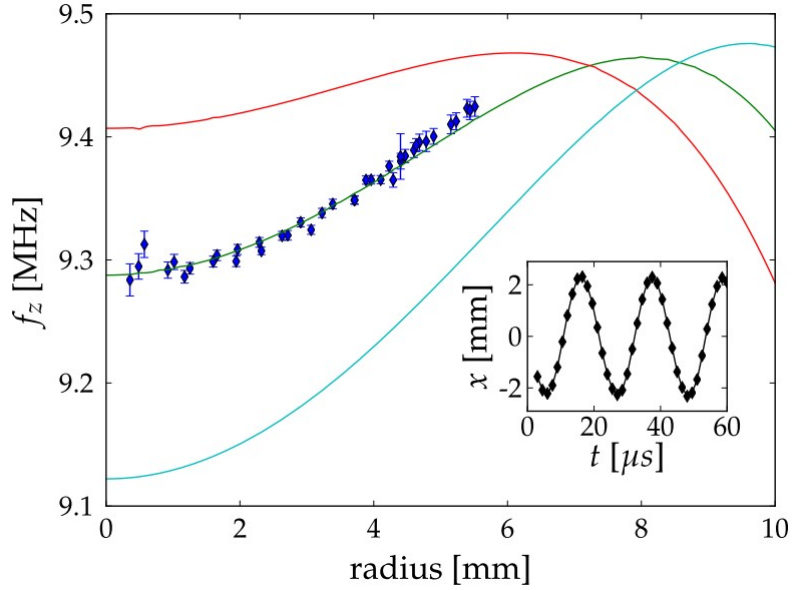
Figure 2.4: Axial bounce frequency, f_z as a function of radial position overlaid with calculations of f_z at three kinetic energies of 100 meV (red), 400 meV (green), and 700 meV (cyan). The inset shows the sinusoidal fit to data that extracts f_z. [25].

trap, it is a variant of the cylindrical electrode Penning-Malmberg trap design used to achieve confinement and accumulation of positrons with an electrode modification and the addition of a low-density molecular 'buffer' gas to provide an energy-loss mechanism.

The original design by Surko, visible in figure 2.5, employed a ^{58}Co radioisotope positron source with a reflective tungsten moderator producing a flux of $8 \times 10^7 \, \mathrm{e^+ \, s^{-1}}$ with energies of $2.5 \pm 1 \, \mathrm{eV}$. These 'slow' positrons were emitted as a beam into the first of 2 stages containing a 'buffer' gas: the first for trapping, the second for accumulation and storage. Since introducing a gas to the positrons will inevitably result in an increase in the positron annihilation rate, a buffer gas trap typically consists of successively lower pressure regions facilitated by larger diameter electrode stages and differential pumping. The first, higher-pressure stage with comparatively smaller diameter electrodes contained a buffer gas of a composition and pressure chosen such that the positrons would lose sufficient energy and become trapped during a single pass. The overall length of the first stage is also chosen to this effect. This is ideally achieved through inelastic scattering via electronic excitation of the buffer gas molecule, typically molecular nitrogen, N_2. In conjunction with a stepped potential applied across the electrode structure, an example of which can be seen in figure 3.6, a potential well of lower energy positrons can be achieved in the second stage.
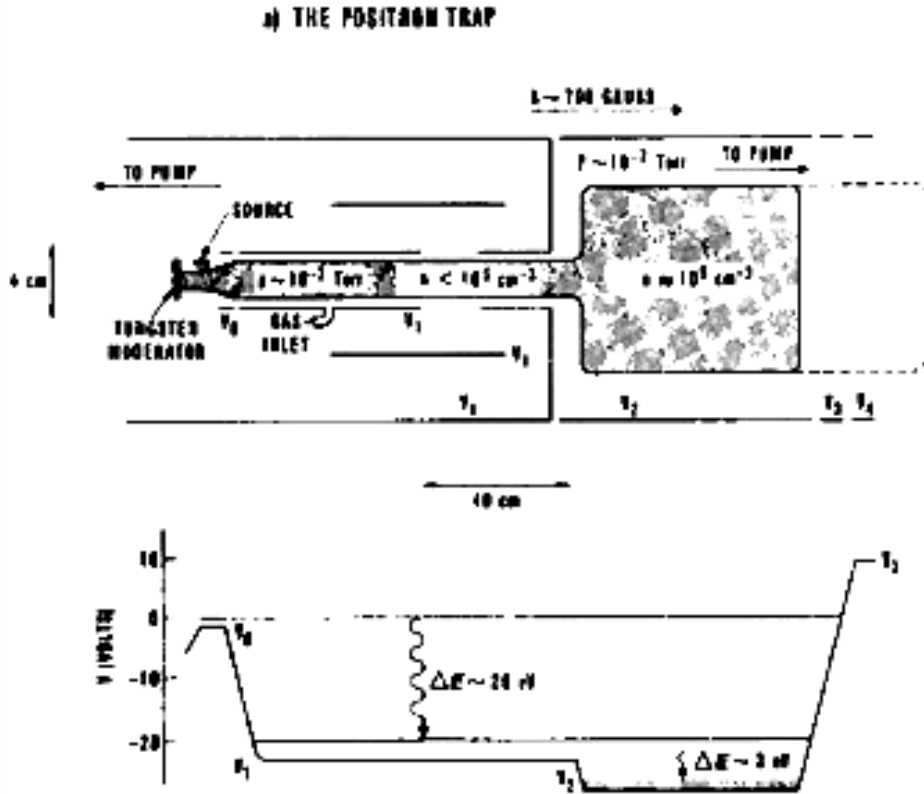
Figure 2.5: Extracted from [32]. Diagram of the original 2-stage buffer gas trap design by Surko et al.

2.2.1 Energy Loss Mechanisms & Positron Accumulation

As a moderated positron enters the buffer gas trap there are several ways it can lose energy upon interaction with a gas molecule such as electronic, vibrational, and rotational excitations with the dominant energy-loss mechanism against a buffer gas being Ps formation, which also results in loss of the positron. These channels will occur at different rates and energy thresholds in accordance with their respective cross-sections, depending on the energy of positron-species interaction.

At lower energies, molecular nitrogen is unique in that its $a^1\Pi_g$ level electronic excited state, where positrons may lose $9\,\text{eV}$ per collision on average, becomes significant at $69,283.06\,\text{cm}^{-1}$ or $8.607\,\text{eV}$ [33]. This is just before the Ps formation threshold of $8.8\,\text{eV}$ and maintains a greater cross-section, up to approximately $11\,\text{eV}$ where Ps formation becomes as efficient at removing positrons as electronic excitation is at trapping them. Therefore, these processes compete with each other, resulting in an energy window or 'trapping gap' of $3\,\text{eV}$ where positron trapping is most favourable. This can be seen directly in figure 2.6.
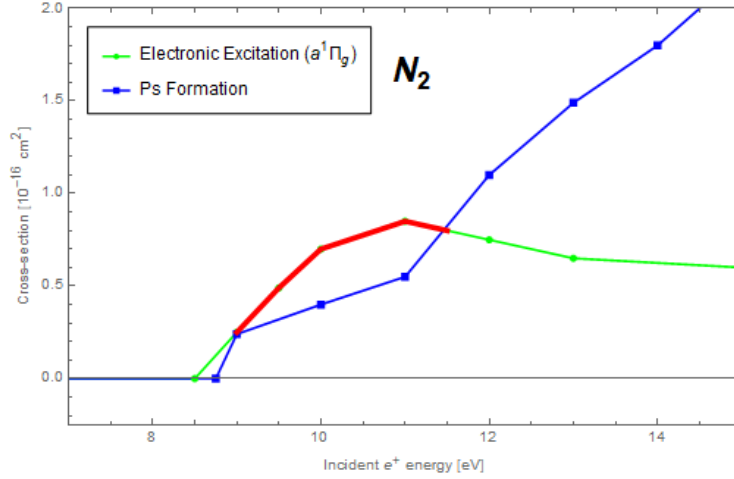
Figure 2.6: Measured cross-sections for the $a^1\Pi_g$ electronic excited state and Ps formation in N_2 as a function of incident positron energy. The optimum energy window for trapping positrons is highlighted in red. Data from [34].

The accumulation of the captured positrons can be described by a rate equation of the following form,

$$\frac{dn}{dt} = R - \frac{t}{\tau} \tag{2.22}$$

where n is the number of positrons, R is the *accumulation rate*, and τ is the *positron lifetime* (the reciprocal of which is the loss rate, λ). This is a differential equation that can be solved to yield a solution for the positron number as a function of accumulation time:

$$n(t) = R\tau \left(1 - e^{-\frac{t}{\tau}}\right) \tag{2.23}$$

where the accumulation rate, R may also be expressed as $I_0\epsilon$; the positron beam intensity and capture efficiency, respectively.

By varying the accumulation time and measuring the number of positrons present at the point of collective annihilation, one can perform a least-squares fit of equation (2.23) to generate an accumulation curve, a common diagnostic measure from which trapping parameters can be extracted and the performance of the accumulator characterised. An example accumulation curve generated from the Swansea apparatus can be seen in figure 2.7. As can be seen in the figure, the trap will fill to an asymptotic saturation point when $t \gg \tau$ i.e., $n_\infty = R\tau$.

For an appropriate buffer gas pressure, positrons of incident energy within the trapping gap will be most efficiently trapped but below the threshold of approximately $8\,\mathrm{eV}$, positrons will most likely equilibrate to room temperature via vibrational and
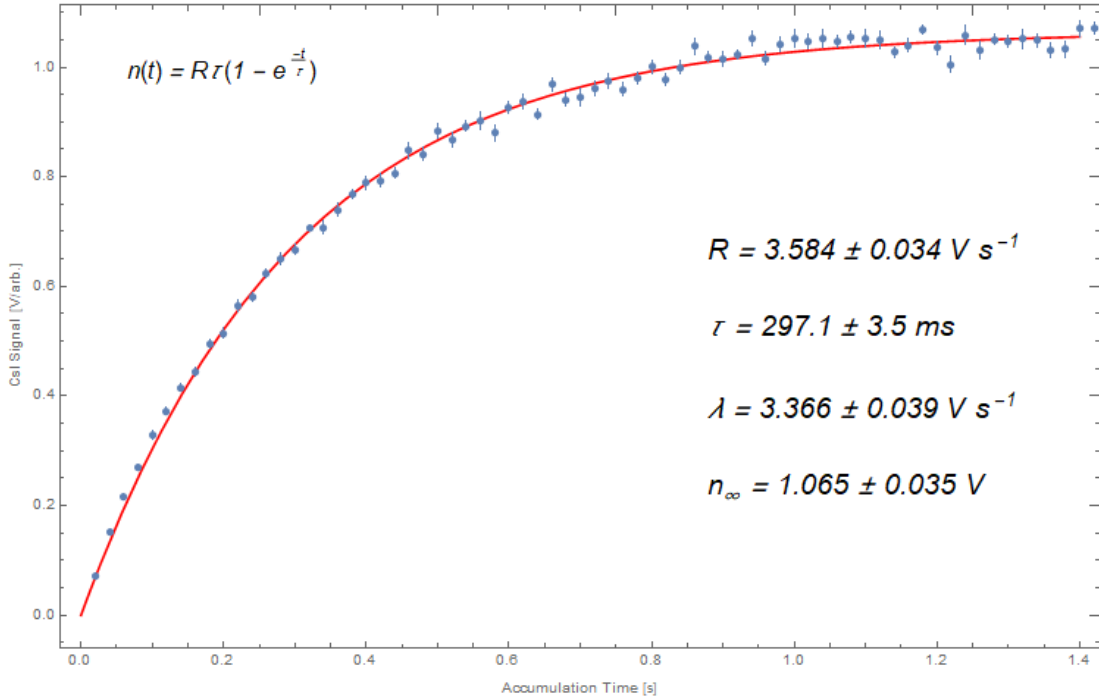
Figure 2.7: An example of an accumulation curve from data generated by the Swansea apparatus. The fitted parameters are R and τ. The fit (equation (2.23)) and the extracted parameters are shown inset.

rotational excitation with the buffer gas. However, as will be seen in section 2.3.2, N_2 is not a very efficient 'cooling' gas.

In a real-world trap, the magnetron orbit is only quasi-stable. If the inherent instabilities are large enough, the repulsive radial term in equation (2.6) will produce a radial diffusion of the positrons that will eventually annihilate on the electrode surfaces. This outward radial transport can be practically eliminated however, and even effectively reversed via induced inward transport of the accumulated positron cloud/plasma.

2.3 Charged Particle Axialisation

As lower energy positrons are accumulated they form a cloud either in the independent ('single-particle') regime or, if the *Debye length*, λ_{De} is sufficiently smaller than all other physical dimensions of the cloud, as a non-neutral plasma. To counteract the undesirable radial expansion exhibited in both regimes and to improve control of the cloud density/magnitude, the so-called "rotating wall" (RW) technique was developed. It involves the application of a rotating electric field with a potential of

the form,

$$V_{\mathrm{RW}}(t) = V_{\mathrm{d}} \sin \left(\omega_{\mathrm{RW}} t + \varphi \right). \tag{2.24}$$

across a segmented cylindrical electrode, as detailed in sections 3.2.4 and 3.2.5, where φ is the phase and V_{d} and ω_{RW} are the applied rotating wall drive amplitude and frequency, respectively.

The technique was first used to radially compress a Mg$^+$ plasma by Huang *et al.* [35] in an effort to improve upon previous counteractive methods such as inducing torque with lasers [36] or traditional sideband cooling [37]. It has since been successfully applied to electron and positron plasma. The method has seen extensive use in increasing positron lifetimes and cloud densities for compact low energy positron accumulators.

Since the Swansea apparatus tends to perform studies on positrons in the independent particle regime as with this study, only a concise overview of the compression mechanism as applies to non-neutral plasma will be provided here. For more detailed information, the reader is directed to [35, 36, 38].

2.3.1   The Rotating Wall - Plasma Regime

A non-neutral plasma confined in a Penning trap will generate an intrinsic radial electric field and effectively spin in the presence of the buffer gas and under the influence of the radially confining magnetic field due to $\mathbf{E} \times \mathbf{B}$ drift with a plasma rotation frequency, ω_{r} given by,

$$\omega_{\mathrm{r}} = \frac{q n_{\mathrm{e}}}{\varepsilon_0 B} \tag{2.25}$$

where n_e is the positron plasma density. The expansion of the plasma due to the slowing rotation can be mitigated by applying a rotating dipole (or quadrupole) electric field which couples to space charge waves inherent in the plasma referred to as Trivelpiece-Gould modes. These are collective plasma oscillations that occur when the charged species in the plasma interact with a magnetic field [39]. This induces a torque in the plasma which can balance the expansion or, depending on the amplitude and frequency of the applied rotating field, result in radial compression. Despite its efficacy in reducing the radial extent of single-component plasmas, the torque induced in the plasma also leads to undesirable heating. To reduce this side

effect, a cooling mechanism is administered. In the case of positrons in a BGT, this typically takes the form of a gas with a relatively high cross-section for inelastic collision processes at low positron energies and low annihilation cross-section such that energy can be removed from the plasma via rotational and vibrational excitation channels.

2.3.2   The Rotating Wall - Independent Particle Regime

If the positron cloud is of insufficient density, it will be considered in the independent particle regime. In this limit, there are no longer Trivelpiece-Gould modes present and therefore this coupling mechanism is no longer viable.

Compression of positrons in this regime towards the trapping centre, or *axialisation*, is achieved via a form of sideband excitation. In 'traditional' sideband excitation, first suggested by Wineland and Dehmelt [37], an oscillating dipole (or quadrupole) electric field is applied to the cloud. However, this form of applied field leads to heating induced by excitation of overlapping sidebands.

In 2008, Greaves and Moxom observed axialisation of a positron cloud in a Penning-type trap by using a rotating quadrupolar electric field, similar to that used for plasmas [40]. In this study the highest central density, and therefore strongest axialisation occurred as the RW frequency approached the axial bounce frequency, ω_z of the trap. They concluded using a plasma-based analysis, that asymmetric bounce resonance was the likely cause. It has since been suggested in [41] however, that the mechanism behind the axialisation of the positron cloud by the RW is due to a different form of motional sideband excitation that only excites a single sideband thus avoiding the inadvertent heating observed when using an oscillating electric field. This is achieved by adding a rotating dipole potential to equation (2.24) where the factored term is rewritten in terms of the axial bounce frequency thus, in Cartesian coordinates,

$$\phi_{\text{rot}}(x, y, z) = \frac{m\omega_z^2}{2q} \left(z^2 - \frac{(x^2 + y^2)}{2} \right) + \frac{m}{q} a z \left(x \cos\left(\omega_{\text{RW}} t \right) - y \sin\left(\omega_{\text{RW}} t \right) \right) \quad (2.26)$$

where a is a term proportional to the applied RW amplitude, V_{d}. A damping term is also added in an attempt to describe the influence of the cooling gas (see below)

on the particles, modelled in this case by a Stokes viscous drag term i.e., $\ddot{\mathbf{x}} = -\kappa\dot{\mathbf{x}}$. By defining a vector coordinate system of the form,

$$\mathbf{V}^{\pm} = \dot{\mathbf{r}} + \omega_{\mp}\hat{\mathbf{z}} \times \mathbf{r} \tag{2.27}$$

Isaac shows in [41] that the magnetron and cyclotron motions are effectively decoupled, and that the analytical solution of the resulting equations of motion for the system,

$$\dot{V}_x^- = \omega_- V_y^- - az\cos\left(\omega_{\mathrm{RW}}t\right) \tag{2.28a}$$

$$\dot{V}_y^- = \omega_- V_x^- - az\sin\left(\omega_{\mathrm{RW}}t\right) \tag{2.28b}$$

$$\ddot{z} = -\omega_z^2 z - \kappa\dot{z} - \frac{a}{\omega_+ - \omega_-}\left[V_y^-\cos\left(\omega_{\mathrm{RW}}t\right) - V_x^-\sin\left(\omega_{\mathrm{RW}}t\right)\right] \tag{2.28c}$$

show that the particles are drawn to the trap axis i.e., axialised at a *characteristic compression rate*, Γ, which is given by,

$$\Gamma = \frac{\kappa}{4}\left(1 - \sqrt{\frac{\left(\omega_{\mathrm{RW}} - \omega_0\right)^2}{\delta^2 + \left(\omega_{\mathrm{RW}} - \omega_0\right)^2}}\right) \tag{2.29}$$

where ω_0 is the upper sideband i.e.,

$$\omega_0 = \omega_z + \omega_- \tag{2.30}$$

and δ is the frequency response width defined as

$$\delta = \frac{a}{\sqrt{\omega_z(\omega_+ - \omega_-)}} \approx \frac{a}{\sqrt{\Omega\omega_z}}. \tag{2.31}$$

Equation (2.29) shows that as the applied RW frequency approaches the upper sideband, the magnetron orbit is reduced, and compression of the positron cloud is maximised i.e., $\Gamma_{\mathrm{max}} = \kappa/4$ when $\omega_{\mathrm{RW}} = \omega_0$. Since this does not make use of the narrow resonances required to avoid overlap of the sidebands, this type of axialisation is applicable to traps with a high degree of anharmonicity including 2-stage BGTs, such as that used in Swansea. For further detail and full derivations, see [41, 42]. Isaac also suggested a differential equation to describe the evolution of the cloud

width, σ, over time by incorporating a *constant expansion term, γ*. This took the following form,

$$\dot{\sigma} = -\Gamma\sigma + \gamma. \tag{2.32}$$

which has the trivial solution of,

$$\sigma(t) = \left(\sigma_0 - \frac{\gamma}{\Gamma}\right)\exp\left(-\Gamma t\right) + \frac{\gamma}{\Gamma}. \tag{2.33}$$

$\sigma_0 = 8.8 \pm 0.3$ mm,
$\Gamma = 67.9 \pm 6.2$ s^{-1},
$\gamma = 118 \pm 19$ mm s^{-1}
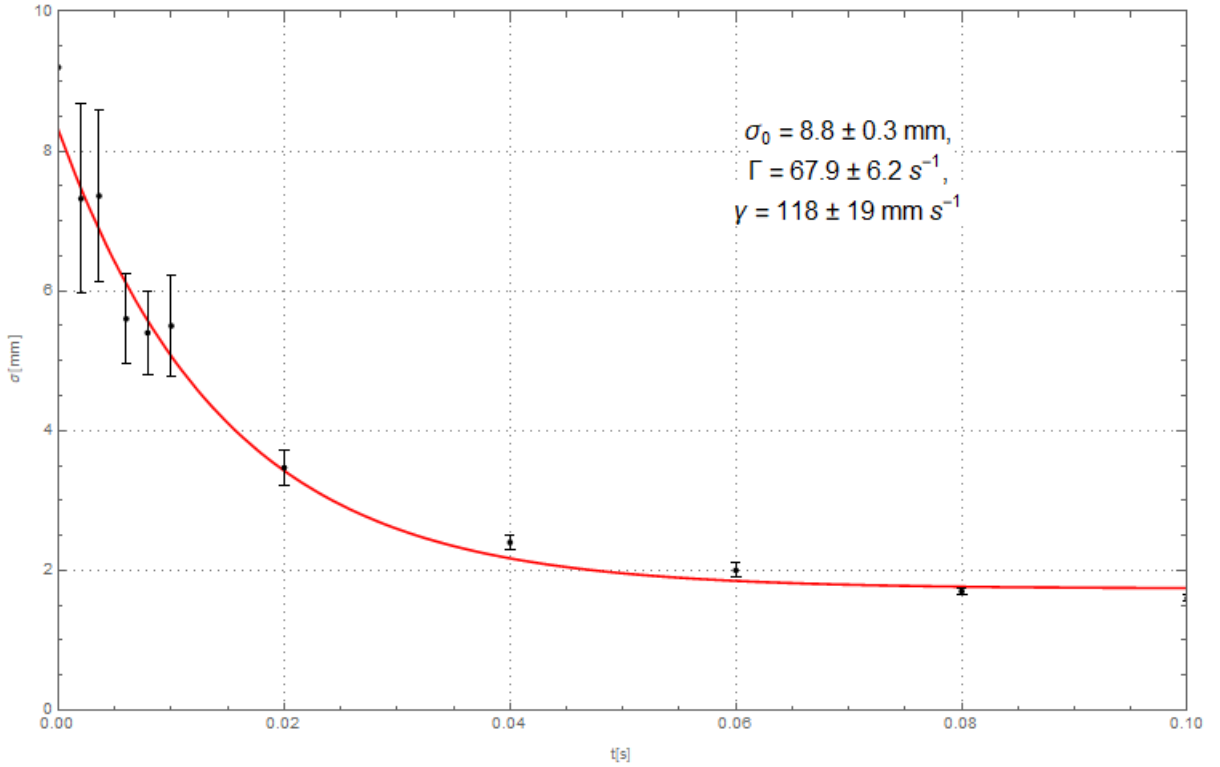
Figure 2.8: An example of a compression curve. The extracted parameters are inset. Data acquired by A. Isaac [43] pp.82

This solution makes several approximations, namely it assumes that the trapping frequencies, and therefore the central frequency of the upper sideband, are constant and that any inherent expansion term is also constant. Despite these approximations however, it provides a fairly good fit to compression curve data. These data can be acquired by varying the length of time the rotating wall is applied to a held positron cloud prior to ejection and detection on a microchannel plate-phosphor apparatus (see section 3.3.2). The radial widths of the clouds are subsequently extracted by applying a 2D Gaussian fitting function to the images captured by a digital camera (see chapter 4). A plotted example of a compression curve can be seen in figure 2.8.

Cooling Gases

Whilst the issue of radial diffusion can be mitigated with the use of the rotating field, the same field also becomes intermittently resonant with the individual particles' motion which induces undesirable heating in the positron cloud. This in turn leads to an increased annihilation rate. Light particles such as positrons will readily lose energy via the emission of cyclotron radiation, however the rate of energy loss or, the cooling time,

$$\tau_{\mathrm{c}} = \frac{3\pi\varepsilon_0 m^3 c^3}{e^4 B^2} \tag{2.34}$$

is strongly dependent on the strength of the surrounding magnetic field. For the 2-stage solenoid typical operational magnetic field of $\sim 38\,\mathrm{mT}$, this gives a cooling time of $> 30\,\mathrm{minutes}$ which is not tenable. Instead, the primary cooling mechanism is achieved via inelastic interactions with a gas.

Trapped positrons will have insufficient energy to make the $\mathrm{a}^1\Pi_{\mathrm{g}}$ electronic excitation channel a viable option and the cross-sections for lower energy processes are comparatively smaller, making N_2 an effective buffer gas but less effective as a cooling gas. It is conducive to use a gas with higher ro-vibrational excitation cross-sections for trapped positrons.

Several gases have been found to meet these criteria and act as efficient cooling gases that can be administered into the vacuum chamber along with the buffer gas. For example, vibrational energy losses from positrons on CF_4 (carbon tetrafluoride) are dominant in the $0.2 - 2\,\mathrm{eV}$ incident positron energy range which is well below the expected Ps formation threshold of approximately $9.4\,\mathrm{eV}$. A comparison of the cross-sections for the antisymmetric 'stretching' mode, σ_{v3} and positronium formation, σ_{Ps} for CF_4 is shown in figure 2.9.
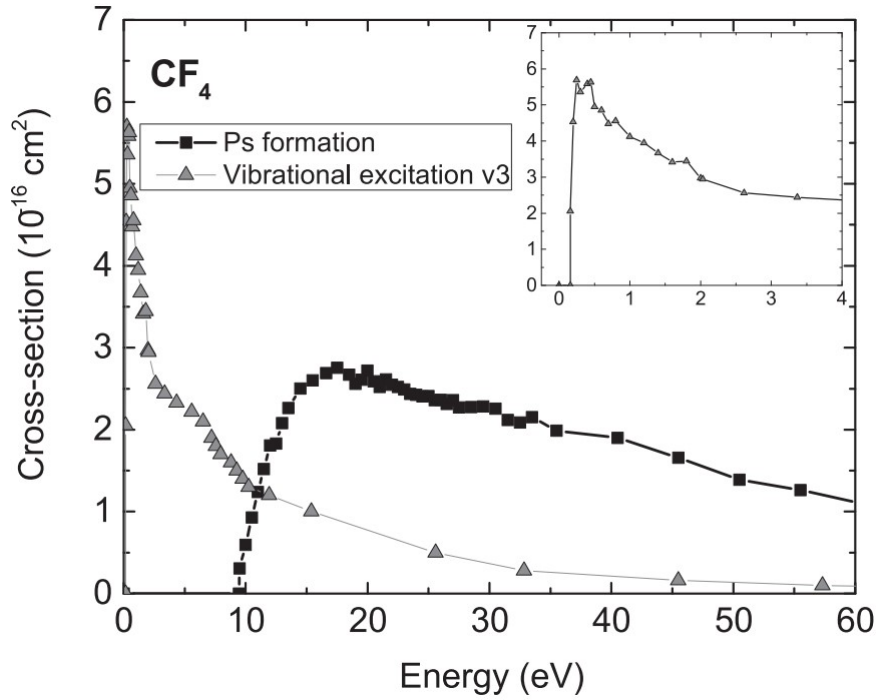
Figure 2.9: A comparison of the measured cross-sections for the ν3 vibrational excitation channel and for Ps formation. The inset shows the first 4 eV of the main plot. Taken from [44].

Positrons of sufficiently low energy could lose 159, 113, or 78 meV per collision for the vibrational excitation states ν3, ν1, and ν4, respectively; ν3 is the strongest channel in this case. The cross-sections of these vibrational interactions need to be higher than those corresponding with N_2 to qualify CF_4 as a more efficient cooling gas and this is indeed the case: a moderated positron with an energy of 10s of electronvolts can be captured after a single e^+-N_2 collision whereas using CF_4 as the buffer gas would require that the same positron undergo multiple collisions before it could become effectively trapped. A table highlighting some pressure-dependent cooling properties of a selection of gases can be found below (table 2.1).

Table 2.1: A selection of gases and their cooling parameters as measured by Greaves and Surko [38] at a pressure of $\sim 2.67 \times 10^{-8}$ mbar in conjunction with a rotating dipole electric field applied to a positron plasma. Present are the cooling and annihilation times (τ_c & τ_A), the energy threshold of vibrational states ($\mathrm{E_v}$), and the plasma compression rate ($\dot{n}/n_\mathrm{max}$).

Formula	Species	$\tau_\mathbf{c}$ [s]	$\tau_\mathbf{A}$ [s]	$\mathbf{E_v}$ [eV]	$\frac{\dot{n}}{n_\mathbf{max}}$ [s^{-1}]
SF_6	sulphur hexafluoride	0.36	2190	0.076, 0.188	10
CF_4	carbon tetrafluoride	1.2	3500	0.157	10
CO_2	carbon dioxide	1.3	3500	0.291, 0.083	4
CO	carbon monoxide	2.1	2400	0.266	<0.02
N_2	diatomic nitrogen	115	6300	0.292	<0.2

2.4   Frequency Chirping

In the compression studies performed by Isaac, Deller, and Mortensen, *et al.* [23, 25], it was confirmed that the axial bounce frequency, ω_z varies with the magnetron orbit/radial position of the positron cloud and used this as a basis to conclude that the less-understood dynamics of compression and heating phenomena would also be a function of radial position.

Using their data and figure 2.4 as an example, we can interpret the following: as compression is achieved for a 700 meV positron at a radius of $\lesssim 10$ mm of the axial trap centre or for a 100 meV positron at a radius $\lesssim 5 - 6$ mm of the axial trap centre, the bounce frequency, and therefore the resonant compression frequency will decrease. From equation (2.29), the aforementioned variation in axial bounce frequency will lead to an altered frequency detuning between ω_0 and the otherwise 'static' applied RW frequency, ω_RW. Deller *et al.*, took the initial phases of the next investigatory step: varying ω_RW as a function of time in order to maintain $\omega_\mathrm{RW} = \omega_0$ and thus keep compression high. This was achieved with a linear frequency sweep function in place of the static frequency, like the one used in this study,

$$\omega_\mathrm{RW} \rightarrow \omega_\mathrm{RW}(t) = \frac{\omega_\mathrm{E} - \omega_\mathrm{S}}{\tau_\mathrm{S}} t + \omega_\mathrm{S}. \tag{2.35}$$

Here the coefficient in front of t is the *sweep/chirp rate*, R_S, and is comprised of τ_s, the *sweep time* i.e., the time taken for the sweep to fully occur, and ω_S and ω_E are

the start and end frequencies of the sweep, respectively.

In the study they varied the end frequency and sweep time whilst measuring the CsI signal and the CCD image intensity from the camera images of the MCP, whilst using SF_6 cooling gas at a pressure of 1.8×10^{-5} mbar. Whilst the study was mostly non-rigorous, they were able to observe a seven-fold increase in areal cloud density using the linear sweep with a lower rotating wall amplitude, V_d, of 0.5 V, when compared to the static frequency case. Density plots showcasing the study can be found in figures 2.10a and 2.10b, and more detail can be found in [25].

(a)

(b)
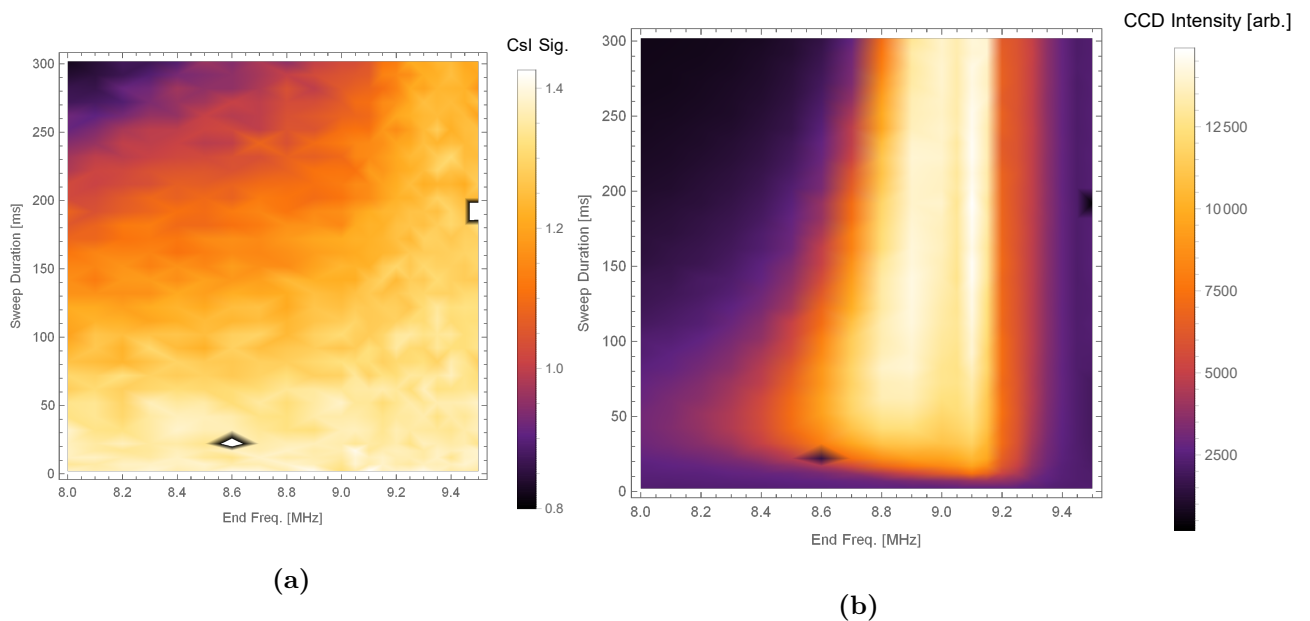
Figure 2.10: Density plots produced Deller in [23] showcasing the short frequency sweep study. (**a**): CsI signal, which can be taken to mean the collective number of positrons in the cloud. (**b**): CCD image intensity which can be taken to mean areal cloud density.

Furthermore, we can now insert equation (2.35) into equation (2.29) to acquire an expression for a time-dependent compression rate that considers the axial bounce frequency's dependency on the distance of the particle from the centre of the trapping axis, r,

$$\Gamma(r,t) = \frac{\kappa}{4}\left(1 - \sqrt{\frac{(R_{\mathrm{S}}t + \omega_{\mathrm{S}} - \omega_0(r))^2}{\delta(r)^2 + (R_{\mathrm{S}}t + \omega_{\mathrm{S}} - \omega_0(r))^2}}\right). \tag{2.36}$$

This further complicates attempts at defining an expression for the cloud width as a function of time due to the increased complexity of introducing a time-varying RW frequency sweep. Increasing our understanding of this is best served by further experimental work and by rough comparison with a simple model, highlighted in chapter 4.

Chapter 3

The Positron Beamline

The positron beamline in Swansea University and its associated extensions, have been extensively and thoroughly detailed in numerous publications and works. This chapter provides a general review of the literature from an experimental standpoint and a technological overview of the current state of the apparatus.

3.1   Brief Experimental History

The design and structure of the positron beamline in Swansea has its origins in both the Surko 2-stage BGT [32] (section 2.2) and the ATHENA (AnTiHydrogEN) project [45] (since disbanded) that was based at the Antiproton Decelerator ring [46] in CERN, some of whose personnel would later form the ALPHA collaboration [47]. The beamline was originally designed to provide the positron density required to produce $\sim 10^4$ Ps atoms when implanted into a silica (SiO) target at $10\,\mathrm{Hz}$ [48]. This was with the overall experimental endeavour of studying Rydberg states of Ps [48, 49]. The beamline receives its positrons from a ^{22}Na β-emitter held inside a moderator cone assembly layered with solid neon as a RGS moderator (see section 1.1.3). Slow, moderated positrons are directed via guiding coils in a quasi-Helmholtz configuration and a transport solenoid to the accumulator which consists of two pressure stages facilitated by differential pumping and two sets of trap electrodes of differing internal diameter housed inside a trap solenoid.

An experimentally devised potential is applied to the trap electrodes in order to

accumulate and then eject a positron cloud onto an annihilation target, the ensuing γ-radiation burst detected via a CsI photodiode detector (see section 3.3). Also present is a Residual Gas Analyser (RGA) for examining the purity of the neon used for moderator growth and a Channeltron Electron Multiplier (CEM) to measure the positron beam intensity. The choice of a compact 2-stage 'Surko' BGT was due to the shorter storage times required. After initially observing odd behaviour in positron flux during moderator growth, it was surmised that the slow positron flux was extremely sensitive to the neon gas purity. Thus, despite a stated purity of 99.999% at the cylinder, an adsorber unit was installed between the neon gas regulator and the moderator chamber to further purify the neon. The adsorber unit contains a highly porous xeolite material with large surface area. Impurities can be frozen out by immersing the unit in liquid nitrogen [50].

As the beamline began producing Ps, several additions were made for specific studies and to expand its functionality. A cryogenic, superconducting 5 T magnet (since removed*) was added at the end of the beamline for studies involving magnetised Ps (results for which can be found in [51]), as well as a laser system with beams crossing the e$^+$-SiO interaction region to perform laser spectroscopy of Ps and excitation to Rydberg states. While the laser system is not the focus of this work, a brief overview of its current status is provided in section 3.2.6.

Since Rydberg-Ps is a potential candidate for efficient production of antihydrogen [52, 53], it is advantageous to be able to reliably produce high quantities of Ps using the beamline, if not to explore and contrast higher excited states with that of hydrogen. Several studies by the group at Swansea have been made to this effect and can be found in [15, 23, 54, 55].

Along with the replacement of the CEM for a microchannel plate (MCP) assembly with phosphor screen in 2011 (see section 3.3) and the addition of a 3rd stage circa 2015, an important prior modification to the beamline was the introduction of the 'rotating wall' achieved via a segmented 2nd stage (and later 3rd stage) electrode. The implementation of this method is elucidated below in section 3.2.5.

---

*The superconducting magnet was eventually transferred to the ALPHA Collaboration to be used as part of an upgrade to their antiproton catching trap.

Extensive studies of positron manipulation using the rotating wall technique have shown that compression of a positron cloud, with appropriate use of a cooling gas to counteract particle heating, is possible and that its use increases the positron lifetime during accumulation, the first evidence for which in the trap, was shown in [54] and reinforced by further experimental work and simulation in [43, 56] whereby the effects of rotating wall amplitude, frequency response width, cooling gas pressure, and the applied magnetic fields were studied. Other groups have also achieved similar results [35, 38]. Subsequently, a successful attempt was made to model the compression/axialisation of positron clouds in the independent particle regime by Isaac *et al.*, in [42] and with more theoretical focus in [41]. This work suggested that the compression mechanism in this regime was a result of a form of motional sideband cooling, unlike reduction of the radial extent of a non-neutral plasma which is achieved by coupling of the rotating field to its inherent Trivelpiece-Gould modes [39], which describe the electrostatic waves along the edge of a magnetised column of plasma. In parallel to these studies, the segmented electrode was utilised by Mortensen *et al.*, [57] to manipulate the magnetron orbit of the positron cloud, thereby extracting the magnetron and axial bounce frequencies as a function of radial position, for a given axial kinetic energy.

In 2014, Deller *et al.*, devised a scheme by which the drive frequency of the rotating dipole could be swept linearly to a variety of end frequencies for a variety of sweep durations [25] in an attempt to address the radial dependence of the axial bounce frequency, ω_z. Whilst this rotating wall frequency chirping allowed for higher density clouds to be produced at lower rotating wall amplitudes, thus requiring less cooling gas, the study was somewhat qualitative and requires further analysis. In particular, comparing the chirp effect on the positron cloud under alternative cooling gases, and comparison of experimental data to a simple model.

3.2 Current Apparatus Status

3.2.1 The Vacuum System

The beamline (see figure 3.1 overleaf) is comprised of a series of five interconnected six-way crosses and a four-way cross surrounding the ^{22}Na source. As with most
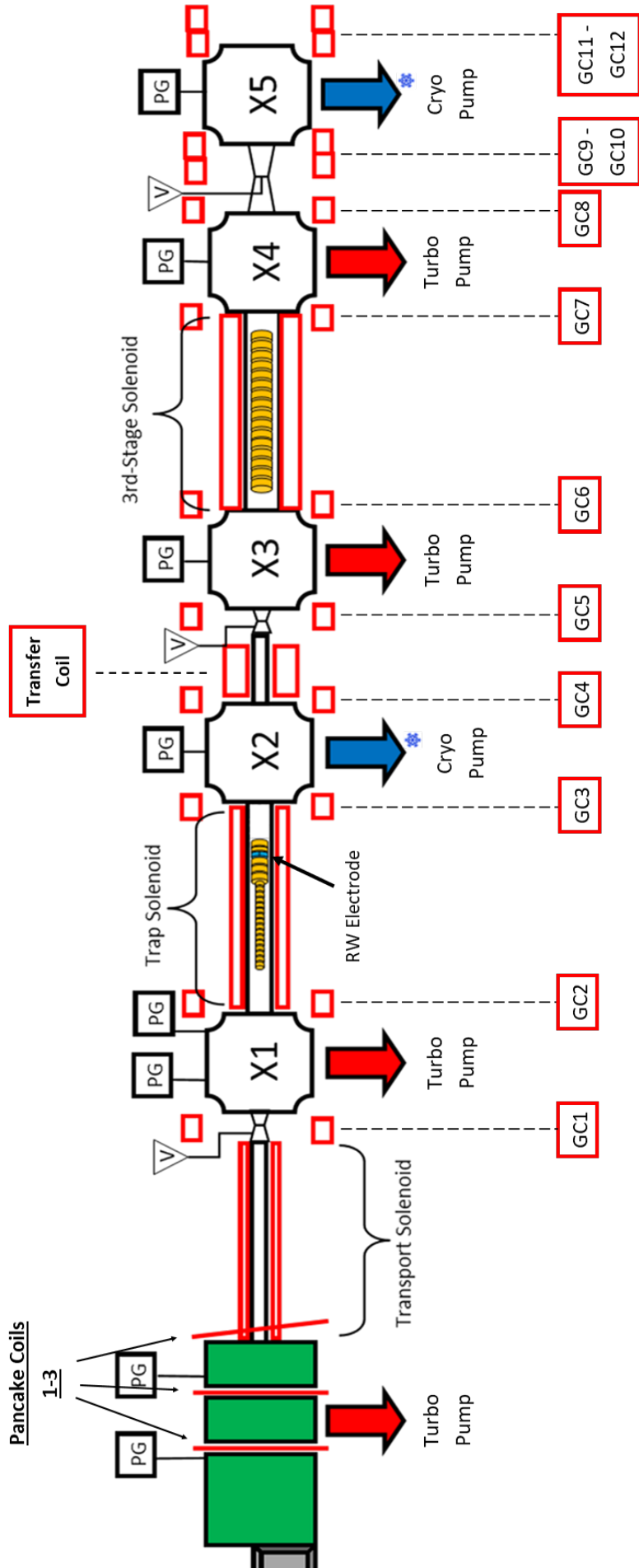
Figure 3.1: An overview diagram of the beamline. Here the guiding coils are labelled **GC#**, the boxes labelled **PG** represent the positioning of pressure gauges, **V** = gate valve, and **X#** = vacuum cross. The 2nd Stage RW electrode is visible in cyan in the 2-stage surrounded by the trap solenoid. The 3rd stage RW electrode is not shown. Not to scale.

particle physics and antimatter experiments, a high degree of vacuum is required to maintain a high mean free path and a reasonable positron lifetime. To this end, the source chamber and vacuum crosses one, three, and four are each actively evacuated by turbomolecular pumps. These pumps feature permanent, 'wear-free' magnetically-levitated bearings on the high vacuum side; the use of oil-free pumps and pumping restrictions on the beamline is paramount since hydrocarbons have an extremely high Z_{eff}, i.e., the charge 'felt' by an electron or positron as it interacts with a multi-electron atom, which would otherwise negatively impact the positron lifetime. The turbopumps are connected to a backing line and are collectively evacuated by several scroll vacuum pumps.

Crosses two and five are evacuated by a pair of cryogenic capture pumps that operate by adsorbing and freezing remaining particulates from a high degree of vacuum and storing them until saturation reduces the pumps' effectiveness. They receive cooled high-pressure helium vapour from a single-stage rotary compressor. As the cryopumps are a form of capture pump, they must be connected to a separate backing or, cryo-roughing line. The cryopumps can then be isolated from the system, opened to the roughing line and brought to room temperature to be regenerated via a separate scroll pump.

In order to continuously monitor the degree of vacuum in the system and backing lines, pressure gauges of several types are positioned at key locations throughout the apparatus. Penning, or cold cathode gauges designed to measure pressure ranges of 10^{-11} - 10^{-2} mbar* are installed on each vacuum cross. Since these gauges can become damaged from their own high voltage discharge at pressures above their operational threshold, an interlock to turn the gauges off exists to protect the hardware. In locations where a lower degree of vacuum is expected such as during moderator growth, a 'Pirani' thermal conductivity gauge is also used to ensure pressure can be constantly monitored; full-range gauges are also useful. Finally, more robust ceramic capacitance gauges are employed at junctions where gases are admitted into the system. Isolation of various parts of the system is accomplished by a multitude of manual full-turn and quarter-turn Swagelok® valves and computer controlled pneumatic-actuated gate valves, while admission of gases can be closely controlled

---

*For air (N_2), although this can vary in practice.

via piezoelectric valves that can be operated manually and via PID controllers.

3.2.2 The Magnets

Positrons are axially confined throughout the entire system with a series of coils and solenoids, some of which require water-cooling due to the high currents used as well as voltage-limited interlocks to prevent catastrophic failure. A table summarising the dimensions and details of the magnets used can be found in table 3.1 while a plot of the magnetic field strength along the beamline can be found in figure 3.2.

Pancake Coils

The epithermal positrons emitted from the RGS moderator are radially confined with a magnetic field produced by three flat coils each consisting of two layers of spirally wound wire sandwiched together that are set amongst the lead radiation shielding. The final source coil (labelled 'Pancake Coil 3' in figure 3.1) is angled and along with a physical axial step in the beamline, acts an energy selector; the positrons' kinetic energy parallel to the trap axis is increased via the source bias but un-moderated positrons that are still too energetic will annihilate on the pumping restriction and be lost while lower energy positrons will be guided over the step and into the first pumping restriction by the angled pancake coil, thereby further narrowing the kinetic energy distribution of the beam. These coils are energised by a power supply nominally providing $\sim 15\,\mathrm{A}$.

Steering Coils & Transfer

A total of 12 steering coils are mounted along the beamline (labelled GC in figure 3.1), situated both upstream and downstream of each vacuum cross in a repeated 'quasi'-Helmholtz configuration in that the coil pairs are wired in series with approximately the same current of $7\,\mathrm{A}$ and that their separation is only approximately the coil radius. Situated at the narrow pumping restriction between vacuum crosses two and three is the fan-cooled transfer coil (also visible in figure 3.1) that provides strong radial confinement to positrons allowing them to pass from the 2-stage trap to the 3rd stage through the narrow pumping restriction. The transfer coil is typically energised with $100\,\mathrm{A}$.

Solenoids

Positrons are radially confined in the trapping and manipulation regions of the system with a set of three water-cooled solenoids. Moderated positrons are guided from the source and into the first vacuum cross by a transport solenoid typically energised with 20-25 A. The 2-stage positron trap and 3rd stage are immersed in a magnetic field provided by the trap solenoid and the 3rd stage solenoid, respectively. These two solenoids are typically provided with 30 A.

Despite the fact that the magnetic field along the apparatus is non-uniform, the axial motion of the positron cloud is generally considered adiabatic due to the reduced velocity of the moderated positrons travelling through the system. From the equation for the magnetic moment of a gyrating particle i.e, the *first adiabatic invariant of plasma physics* [58] which, for the above case is conserved, it can be shown that positrons will mostly follow the magnetic field lines. Therefore the radial extent of the positron cloud will be reduced in high B-field regions and will diverge in low B-field regions i.e, the experimental crosses.

This is important to note, since it means that the radius of a positron cloud in the accumulator (2-stage) will be a factor of approximately 2.6 larger by the time it is detected and imaged by the MCP approximately 2 metres downstream.

Table 3.1: A summary of the dimensions & details of the magnets used along the beamline.

Coil	r_{int} (mm)	r_{ext} (mm)	L_z (mm)	Turns	I (A)
Pancake Coils	72	238	18	160	15
Transport Solenoid	60	68	890	888	25
Trap & 3rd Stage	73	81	680	680	30
Transfer Coil	22	62	103	40	100
Steering Coil	263	300	60	400	6-7
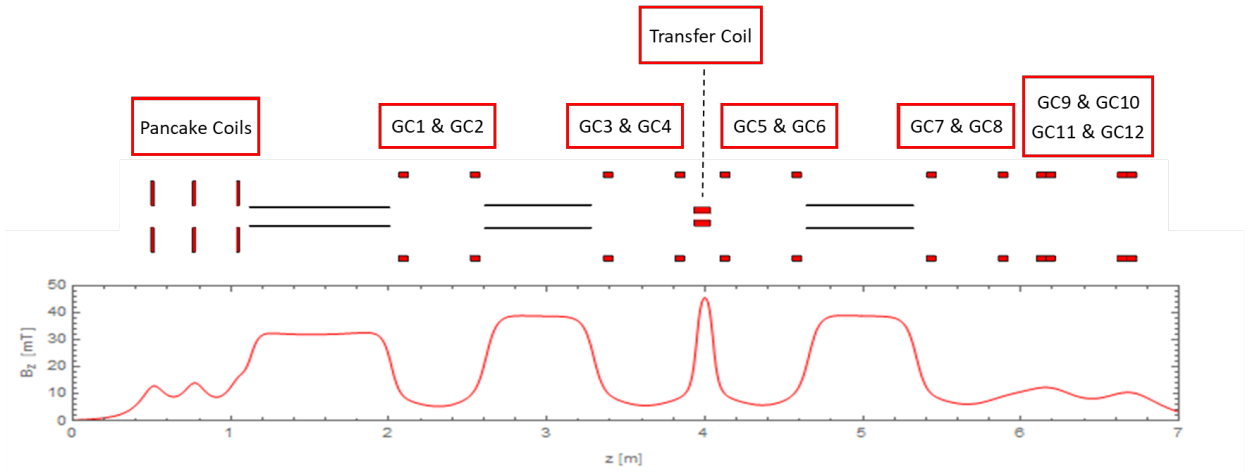
Figure 3.2: The magnetic field strength as a function of axial position on the beamline. Calculated numerically utilising previous work by [23]. The rises in field strength coincide approximately with the position of the magnets as labelled here and in figure 3.1.

3.2.3   The Source

The beamline effectively begins with a sealed ^{22}Na radioisotope positron source manufactured using an evaporative process to produce a desired activity level [59]. The source is deposited onto a capsule lined with high-Z_{eff} materials, namely a titanium foil with tantalum backing. Use of these elements acts to backscatter and direct the emitted positrons such that their overall direction can be controlled.

For installation on the beamline the source capsule, as seen in figure 3.3, is mounted into a source holder fabricated from a tungsten-copper alloy that is electrically isolated from, but thermally coupled to, the system via polyether ether ketone (PEEK) supports, and a sapphire disk, respectively. PEEK is a commonly used, strong, thermoplastic polymer that allows the source to be biased and therefore the energy and intensity of the positron beam to be adjusted. The sapphire disk acts as a coupling between the source holder and the coldfinger of a cold head that receives cooled high-pressure helium vapour from a three-phase compressor. This arrangement allows the source to reach temperatures as low as $5.7\,\mathrm{K}$ [60] as measured by a chromel-AuFe alloy thermocouple attached to the source holder. The temperature of the source can also be directly controlled by use of a temperature controller attached to a small electric heating element at the base of the source holder; this is particularly useful for hastening the removal of a moderator for regrowth or, at lower power ($500\,\mathrm{mW}$) can be used for moderator annealing. Finally, the front of the source capsule is
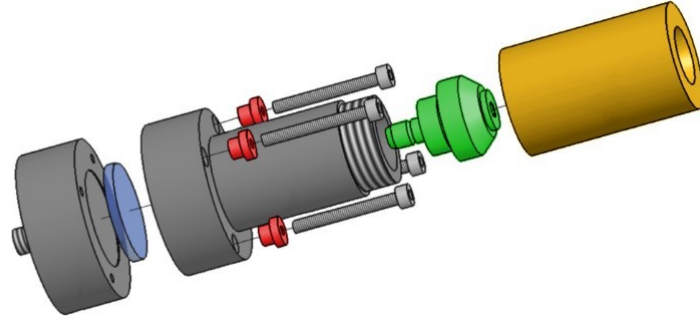
Figure 3.3: An exploded CAD model of the source assembly. The moderator cone (gold) screws onto the source assembly (green) which in turn screws into the source holder. The sapphire disk (blue) and PEEK supports (red) are visible. Taken from [43].

screwed into a copper 'moderator cone' that features an inverted cone of 15.7° half-angle; Khatri et al., demonstrated in [61] that a conical shape improved emission of moderated positrons.

The entire assembly is housed inside the four-way vacuum cross and surrounded by an appropriate amount of lead radiation shielding as well the three flat source 'pancake' coils (figure 3.1).

3.2.4 The 2-Stage Buffer Gas Trap

After positrons are emitted from the ^{22}Na source they will interact with the solid neon film and a fraction will be re-emitted as moderated positrons as briefly described in section 1.1.3. The pancake coils prevent these positrons from escaping with a field strength of approximately $30\,\text{mT}$ and guide them approximately two metres downstream through the transport solenoid, the first six-way cross enclosed by a pair of guiding coils in quasi-Helmholtz configuration and into the trapping region.

Electrodes

The 2-stage accumulator contains a set of 22 electrodes, all of which can be seen in figure 3.4 and is comprised of a gate electrode and a subset of 15 stacked Au-plated aluminium electrodes each approximately $24\,\text{mm}$ in length, with an inner diameter of $16\,\text{mm}$ and electrically insulated from each other by $2\,\text{mm}$ sapphire spheres. The ends of the electrodes are indented such that they can fit closely together and the
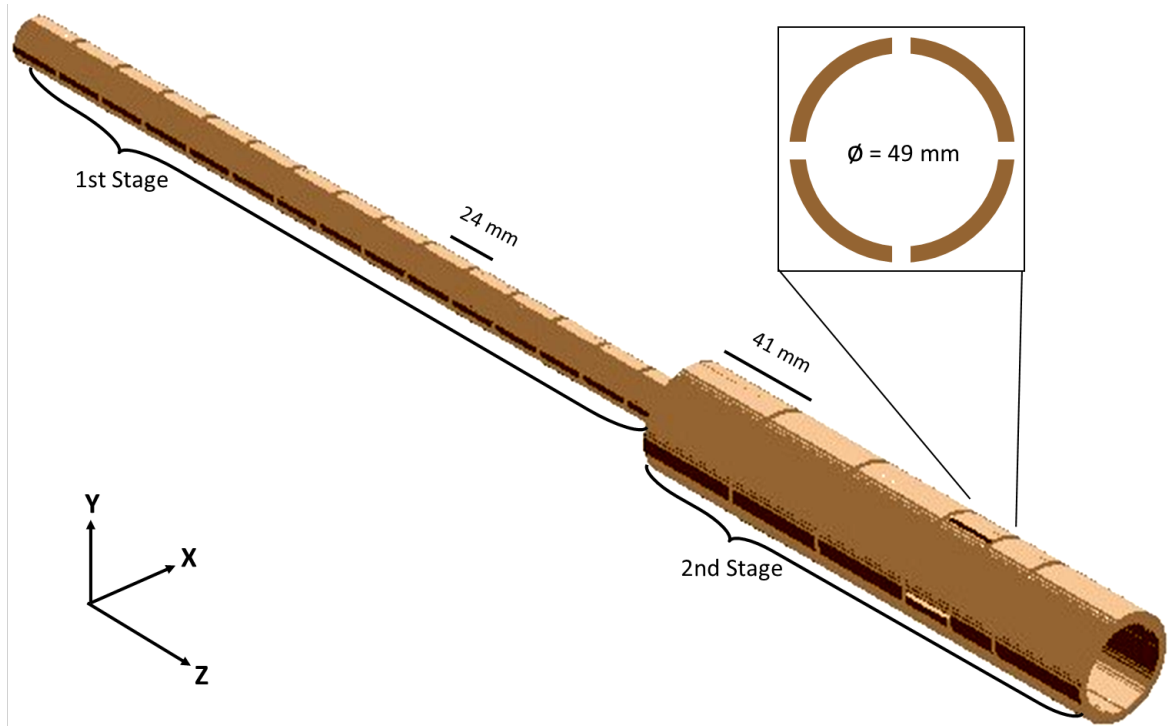
Figure 3.4: A model of the 2-Stage electrode structure rendered using SimION®. This stacked assembly sits inside 2nd stage. The azimuthally segmented 'rotating wall' electrode is visible near the bottom right. Inset: Axial view of rotating wall electrode.
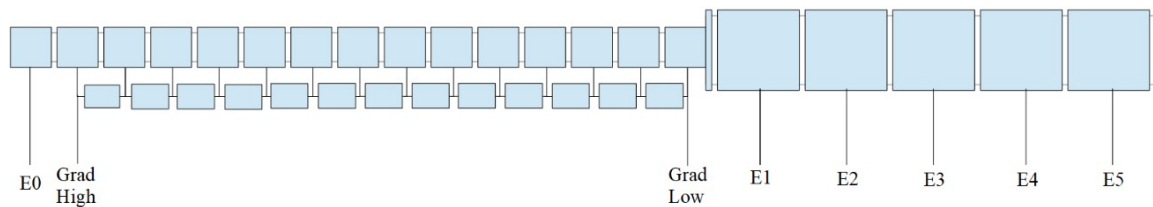
Figure 3.5: A diagram of the 2nd stage electrodes and the 8 electrical connections made after grouping most of the 1st stage with a resistor chain to create a gradient. Taken from [62].

8th electrode features a dorsal inlet where the buffer gas, usually molecular N$_2$ can be administered. The 2nd stage is comprised of four electrodes of approximately 41 mm length and an inner diameter of 49 mm while the 5th electrode (4th sequentially) is halved axially and one of these halves is azimuthally segmented as to create four quadrants, visible in figure 3.4. This is the 'rotating wall' electrode.

The trap solenoid radially confines the positrons with a field of approximately 35 mT and are confined axially by applying appropriate potentials to each of the electrodes. A resistor chain housed in an external box allows for a potential gradient, typically 1-2 V to be applied across the 1st stage while each of the 2nd stage electrodes can be independently set in a 'DC' mode with the option of superimposing a rotating dipole onto the segmented electrode. A typical accumulation sequence, set and triggered via computer control for a source bias of 50 V (see section 3.4) may look like Table 3.2.

Table 3.2: A typical accumulation sequence consisting of three steps. Each step showing the potentials applied to each electrode.

	Gate	Grad Low	Grad High	E1	E2	E3	E4	E5
Catch	45 V	44 V	38 V	35 V	34 V	33 V	28 V	140 V
Hold	140 V	44 V	38 V	35 V	34 V	33 V	28 V	140 V
Eject	140 V	44 V	38 V	35 V	34 V	33 V	28 V	0 V

And visualised in figure 3.6, thus:
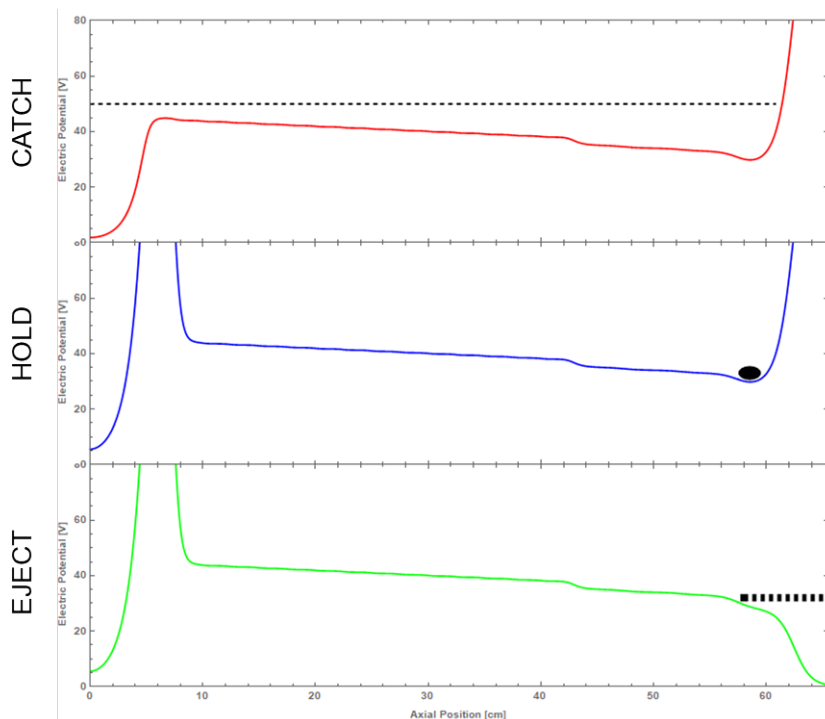
Figure 3.6: A plot of the stepped potential accumulation sequence described in the table above. The black dashed line and elliptic disc represents a moderated 50 V positron beam and accumulated positron cloud, respectively.

A cloud of positrons accumulated and ejected using the sequence in table 3.2 will then travel into cross 2 (X2).

X2 is where the vacuum feedthroughs are located that permit both the buffer and cooling gases to enter the trap. The top flange of this cross (and all others) usually holds some piece of equipment attached to a manually operated linear manipulator to move apparatus in and out of the beam path such as a stainless steel plate to act as an annihilation target, an electron source for requisite studies (typically housed in cross three), a silica-based Ps converter assembly (held in cross five to coincide with the laser beam paths) or, more recently, a silicon carbide (SiC) assembly for studying re-moderation.

3.2.5 Rotating Wall Implementation & The Magnetron Kick

When only simple accumulation on a buffer gas is desired, both halves of the split electrode, including all four quadrants of the segmented electrode, may have the same static potential applied. When compression of the positron cloud is required or some other particle manipulation desirable, the azimuthally segmented electrode
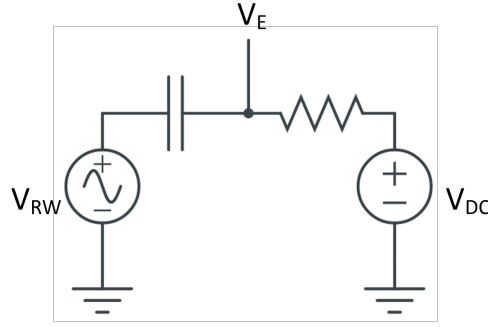
Figure 3.7: A rough basic schematic of the high-pass filter used to superimpose the static, "DC" voltage and the "rotating wall" AC signal produced by the multifunction synthesiser/phase splitter scheme. V_E would take the form of equation (2.24) with the addition of the static voltage when the rotating dipole is employed.

may be utilised.

Parameterisation of the rotating wall application may be specified using the control software (information on the hardware and how the computer control scheme allows for control of the potential can be found in section 3.4) transmitted via GPIB (General Purpose Interface Bus) to a Wavefactory multifunction synthesiser. For static compression i.e., rotating wall compression with a single drive frequency, ω_{RW}, a function of the form of equation (2.24) is generated and supplied to two signal outputs of the Wavefactory with a phase offset of $\frac{\pi}{2}$. These two sinusoidal voltage signals will, to a certain tolerance, be phase-locked with each other, carrying a relative phase difference of $\frac{\pi}{2}$ radians to produce the dipole.

For a rotating dipole to be achieved, each quadrant of the segmented electrode must receive an individual signal with a phase offset of exactly $\frac{\pi}{2}$ to adjacent electrodes, i.e., in quadrature. To this end, the two phase-locked signals are passed through a series of coaxial two-way phase splitters and inverted to obtain four rotating wall electrode segment signals, each $\frac{\pi}{2}$ out of phase. A high-pass filter circuit, the likes of which can be seen in figure 3.7, is then employed to superimpose the signals onto the segments along with the chosen static potential for trapping and accumulation. A software-based correction is administered to the chosen amplitude to account for attenuation brought forth by the post-Wavefactory hardware. Analysis of the rotating near-dipole field that results at the electrodes has been done elsewhere in [23] by solving the Laplace equation and can be seen schematically in figure 3.8.

The amplitude and frequency of the rotating wall can be set and varied with appropriate sequencing in conjunction with accumulation to produce a dense cloud

of positrons to be collectively annihilated whereby the annihilation signal can be detected further downstream via a scintillation detector. Since the application of the rotating field can lead to losses from induced heating, a sufficient quantity of cooling gas is administered into cross two of the system via Swagelok piping and a piezoelectric valve along a separate channel to the buffer gas. The valve is controlled using a PID algorithm from a LabVIEW® program to generate a stable pressure profile which can be scaled by increasing or decreasing the set-point voltages; the same control mechanism is applied to the buffer gas entering the trap.
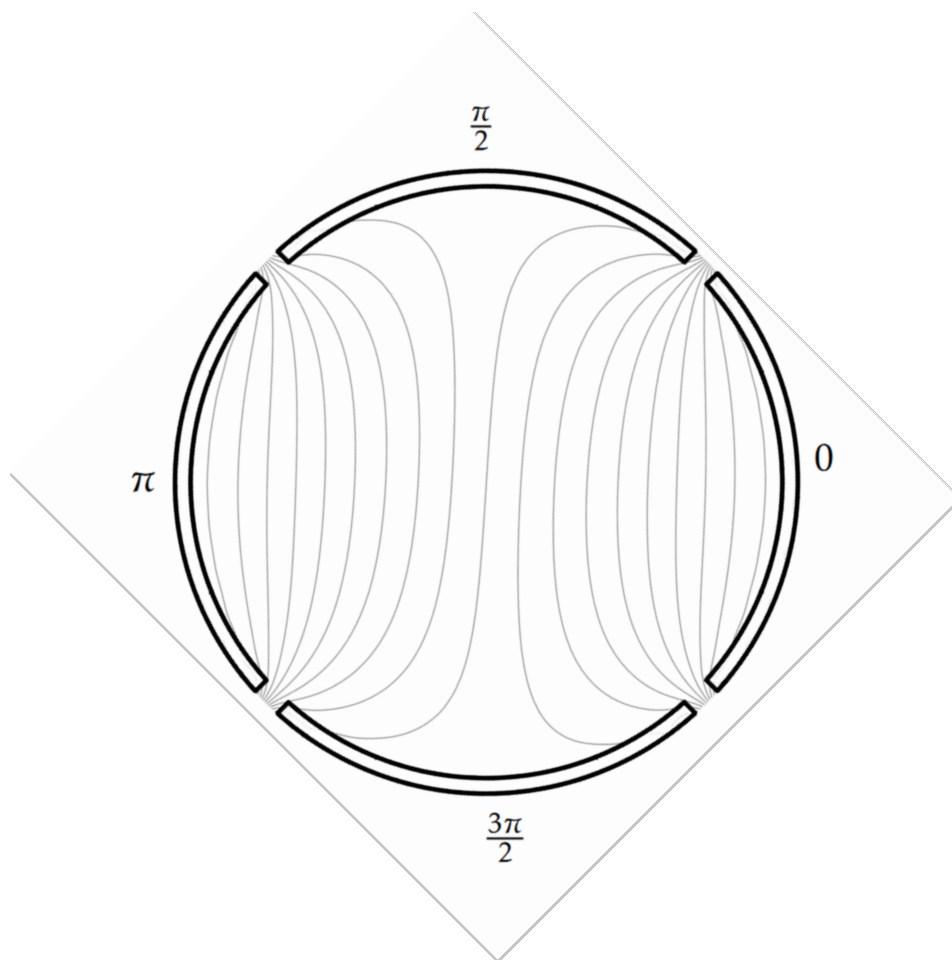
Figure 3.8: A diagram of the four-segment electrode with the rotating dipole applied. The field lines are based on an approximate solution to the Laplace equation using Fourier series expansion. The phase value for each segment is shown. Taken from [23] pp.43.

Sweep Operation

Whilst the Wavefactory is capable of administering drive frequencies in the range of 0.01 µHz - 15 MHz, it is also capable of performing either a linear or logarithmic gated frequency sweep with a sweep duration resolution of 1 ms, thus implementing
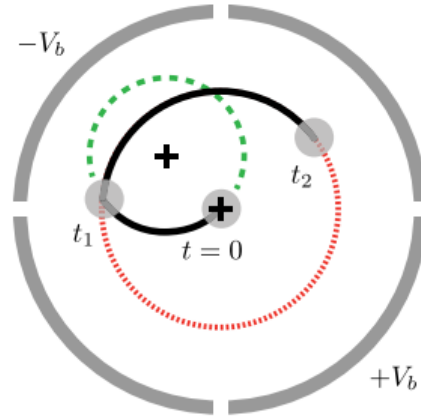
Figure 3.9: Schematic of the 'magnetron kick' in use. The green dashed line denotes the orbital motion during application of the magnetron kick from t_0 to t_1, while the red dotted line represents the new orbit of the positron cloud (grey circle) until the cloud is ejected at t_2. From [57]

the frequency sweep described in section 2.4. This mode of operation requires only an alternate program to run; no hardware modifications are necessary.

Magnetron Kick

The configuration of the segmented electrode also allows for the application of a static radial dipole field which, in the single-particle regime, serves to shift the orbital motion of a compressed positron cloud off-axis without a significant level of expansion.

This is possible because the expansion rate of the positron cloud upon switching off the rotating wall is small compared to the magnetron orbit frequency. A more detailed theoretical breakdown can be found in [24, 57].

Utilising the segmented electrode in this way provides the ability to control the radial position of the positron cloud upon ejection which proves useful for extracting the magnetron frequency, ω_- and thus the axial bounce frequency, ω_z provided that the cyclotron frequency, Ω_c is known, as is performed experimentally in [25].

3.2.6 The 3$^{\text{rd}}$ Stage & Laser System

The lower pressure 3$^{\text{rd}}$ stage extends the system to facilitate increased lifetime of the trapped positrons and can be used as a 'buncher' to reduce the temporal width of the cloud. Surrounded by another water-cooled solenoid, the electrodes here are
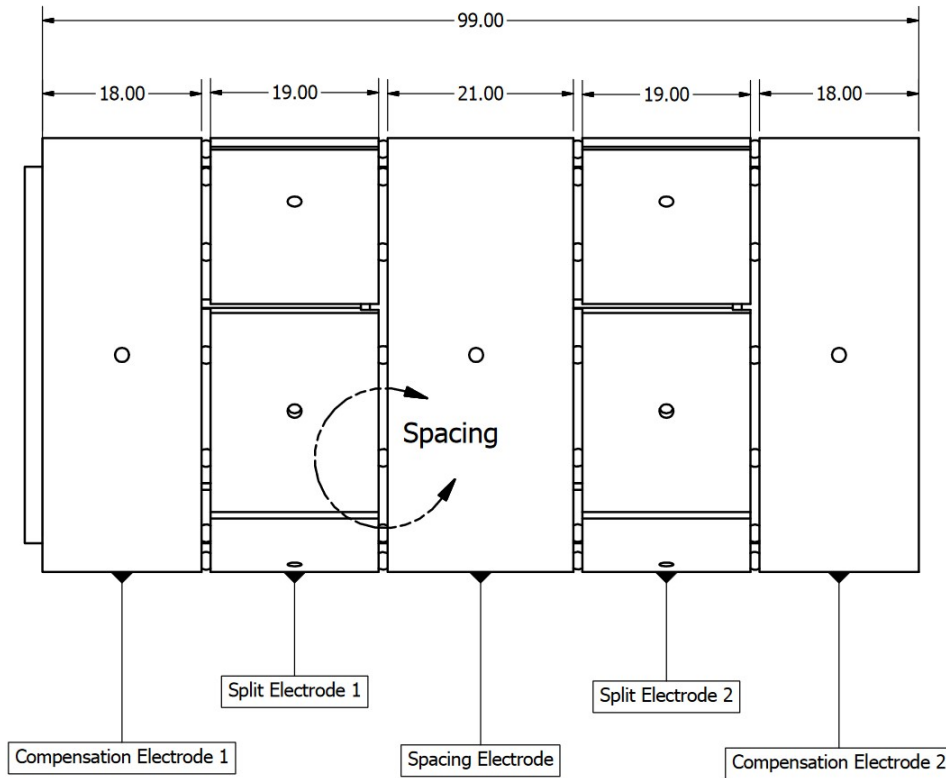
Figure 3.10: A schematic of several 3$^{\text{rd}}$ stage electrodes including the six-segment pair. Taken from a schematic produced by [63].

of internal diameter 41 mm as the 2$^{\text{nd}}$ stage electrodes are but of varying lengths to produce a harmonic well between a pair of six-segment rotating wall electrodes as seen in figures 3.11a & 3.11b allowing for further experimentation with the rotating wall. When these electrodes are not being utilised for cloud manipulation, the 3$^{\text{rd}}$ stage serves to convey the positron clouds ejected from the 2-stage trap downstream to crosses four and five to interact with the MCP or another experimental region such as the Ps converter.

Ps Converter & Rydberg-Excitation Laser

The system currently produces low-energy Ps using a custom-built converter assembly attached to a linear manipulator in cross five (X5 in figure 3.1) consisting of an alignment electrode, a grid, and a mesoporous SiO target, all of which can be biased independently; the latter is implanted with a compressed positron cloud producing o-Ps with an estimated efficiency of approximately 30% [55]. Since Ps does not form part of the present study, a more thorough description of the assembly and spectroscopic studies utilising it can be found in [23, 55, 62].
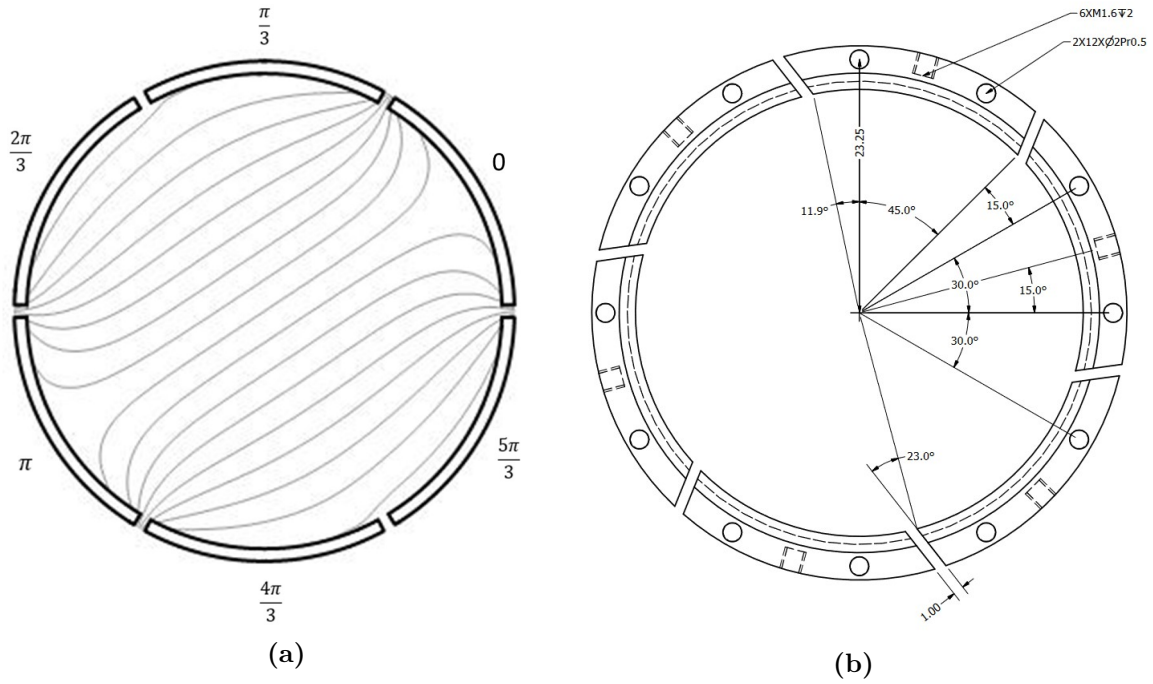
Figure 3.11: Cross-sectional views of the six-segment rotating wall electrode employed in the 3$^{\text{rd}}$ stage with **(a)** exhibiting field lines and a dimensional schematic in **(b)**. Taken from [23] and [63], respectively.

X5 is also the region where the beams produced by the laser system converge (figure 3.12) which is used to perform laser spectroscopy of Ps and to produce Rydberg-Ps.

3.3 Detection Methods

A number of detectors are utilised along and around the beamline to indirectly detect electron-positron annihilations. Several detector types are used depending on the nature of the required measurement e.g., estimating positron number or measuring the radial extent and imaged intensity of a positron cloud.

3.3.1 Scintillation Detectors

A scintillator is a material that scintillates i.e., luminesces when excited by ionising radiation and are utilised for detecting the gamma rays produced during positron-electron annihilations. No single material exists to satisfy what constitutes an *ideal* scintillator, but a gamma ray scintillator may be expected to possess the following properties [13]:
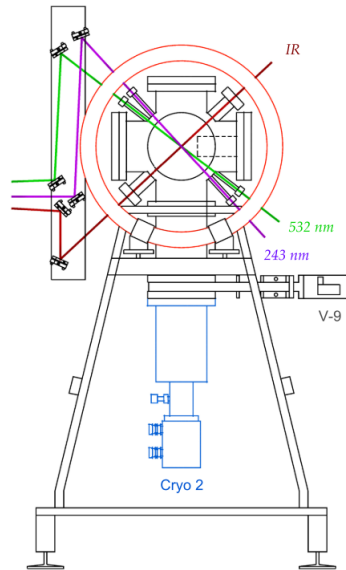
Figure 3.12: A cross-section of the DN160 ConFlat stainless steel six-way vacuum cross that houses the Ps converter. The additional optical feedthroughs with laser beams can be seen. Taken from [23] pp.73.

- High scintillation efficiency i.e., strong linear conversion of incident radiation/particle kinetic energy to a detectable light emission whilst the material remains mostly transparent to it's own emission radiation to maximise luminosity (light yield).

- A high density (or Z number) to maximise absorption.

- The decay time of the induced luminescence should be very short to enable the generation of fast pulses.

- The refractive index of the scintillator material should ideally match or be close to a suitable glass or acrylic material to enable efficient coupling of the scintillation luminescence with a sensor such as a photodetector or photomultiplier tube.

Scintillators can be classified primarily according to whether they are organic or inorganic, with the specific detection medium chosen to suit the incident radiation/particle to be detected. Organic scintillators like various plastic polymers and liquid solvents tend to have a fast response but in general have a reduced light output whereas inorganics tend to have a higher light yield and are generally relatively slow [13]. While many organic and inorganic scintillator materials exist for various

applications in many forms, an inorganic crystal is better suited for positron-electron annihilation gamma ray detection due to its high density i.e., high-Z number. For optimum gamma ray detection, a high-Z material will favour photoelectric processes, for which the cross section scales as Z^{5*} [13].

When an inorganic scintillation crystal such as an alkali-metal halide absorbs energy, a hole is created as an electron is excited across the energy band gap from the valence band to the conduction band, after which it will relax back to its previous state and release a photon [13]. These photons tend to have a peak emission wavelength outside of the visible spectrum and thus *activator* impurities may be added to modify the energy band structure of the crystal lattice, allowing for energy states to be created within the *forbidden* region of the band gap, visualised in figure 3.13. This allows for prompt fluorescence in the visible spectrum which leads to simpler detection via photodetector.
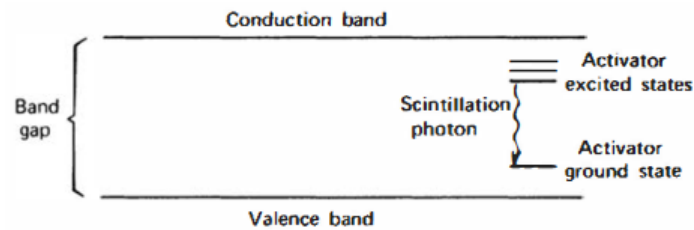
Figure 3.13: Energy band diagram of a doped crystal scintillator. Taken from [13] pp.235.

This work primarily makes use of two varieties of alkali-metal halide crystal scintillation detectors, CsI(Tl) and NaI(Tl) while the beamline also makes use of the fast scintillators $PbWO_4$ (lead tungstate) and LYSO (lutetium-yttrium oxyorthosilicate) coupled to photomultiplier tubes for detecting excited states of Ps. A summary of these detectors is shown in table 3.3.

NaI(Tl) & Counting Mode

Thallium-doped sodium iodide (NaI(Tl)) is used near the source end of the apparatus, generally stationed directly beneath the first steering coil upstream of vacuum cross 1, primarily for moderator characterisation during growth and for monitoring the positron beam. CsI(Tl) can also be used for this purpose but has less desirable

---

*At higher gamma ray photon energies ($>5\,MeV$) pair production dominates.

timing characteristics (see table 3.3) and would thus involve recalibration due to altered detector efficiency. For effective use as a scintillation counter, the NaI(Tl) crystal is coupled to a photomultiplier tube (PMT) by a bialkali photocathode able to detect photons around the peak emission wavelength of 415 nm upon which, the primary photoelectron emitted initiates secondary electron cascades via a series of dynodes which are collected at the anode. The amplified signal generated by the PMT is then sent to a time spectroscopy amplifier which also provides pre-amplifier power to the portable CsI(Tl) detectors. The number of primary photoelectrons emitted by the photocathode in the PMT is proportional to the energy of the incident gamma ray absorbed by the scintillator. Therefore, after amplification at the anode of the PMT, the size of the electric current will also be principally dependent on the energy of the original gamma ray photon.

CsI(Tl) & Pulse Mode

Whereas the counting mode is aimed at singular annihilation events, there are occasions when detecting the annihilation photons from a large group of positrons, i.e. a cloud, at once are necessary. This is always employed after accumulation to garner information about the accumulator's performance and can be used in conjunction with the count rate at known calibration points on the beamline to relate the signal amplitude on an accumulation curve, to positron number, N_{e+}. Whilst not as useful for fast counting applications, thallium-doped caesium iodide (CsI(Tl)) is quite rugged, more resilient to radiation damage than NaI(Tl) and produces greater luminosity.

The two CsI(Tl) scintillators used on the apparatus are not coupled to PMTs, instead they are lightweight scintillator/silicon photodiode devices with pre-amplifiers that can be mounted directly onto and amongst parts of the beamline such as on the six-way vacuum crosses. These are powered via independent battery packs and their output signals are generally recorded via a *National Instruments* PCI-5152 digitiser expansion card and measured by a LabVIEW virtual instrument program. When a positron cloud is accumulated and ejected onto an annihilation target, there will be a 'pulse' of positron annihilation radiation. The rise time of the CsI(Tl) detector is slow compared to the time taken for the photons to be detected from the annihila-

tions, such that the signal generated by the CsI(Tl) detector will be proportional to the number of positron dumped. As a result, the estimated number of positrons in a cloud can be related to the measured pulse height, P_{D}, by

$$N_{e^+} = \frac{P_{\mathrm{D}}}{G \varepsilon_{\mathrm{D}} A_{e^+}} \tag{3.1}$$

where G is the amplifier gain, ε_{D} is the total efficiency of the detector, and A_{e^+} is the average CsI(Tl) signal associated with detection of a single positron-electron annihilation event that can be obtained over many measurements. For imaging and measuring the spatial distribution of positron clouds, an MCP is used.

Table 3.3: Summary of properties of scintillators used on the apparatus. Where $L_{\mathbf{I}}$ = luminosity, τ = prompt fluorescence decay time, $\lambda_{\mathbf{max}}$ = peak emission wavelength, ρ = material density. Informed by [23, 64].

Detector	$L_{\mathbf{I}}(\gamma/\mathbf{keV})$	$\tau(\mathbf{ns})$	$\lambda_{\mathbf{max}}(\mathbf{nm})$	ρ $(\mathbf{kg/m^3})$
NaI(Tl)	44	250	415	3670
CsI(Tl)	56	980	530	4510
PbWO$_4$	0.2	6	420	8280
LYSO	33	36	420	7100

3.3.2 MCP & Phosphor Imaging Assembly

Attached to a linear manipulator and housed in vacuum cross four (X4), is a chevron detector assembly containing two microchannel plates and a phosphor screen assembly, a model of which can be seen in figure 3.14.
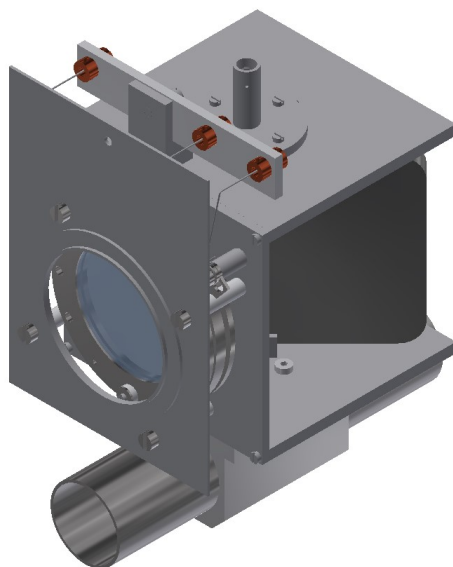
Figure 3.14: A CAD model of the MCP-phosphor assembly with the accelerator visible beneath. Taken from a model produced by [65]

The MCP assembly consists of a pair of stainless steel plates sandwiched together with their exterior surfaces coated in a conductive substance. Both plates are fully perforated with many millions of holes of $10\,\mu m$ diameter and a $12\,\mu m$ hole centre-to-centre spacing, nominally. Each of these holes is approximately 8° from the normal and the plates are rotated 180° from each other. This is a common electron multiplier arrangement for MCP plates that facilitates enhanced gain and prevents feedback.

These plates emit a cascade of electrons that impinge on a P43 phosphor; a $Gd_2O_2S(Tb)$ screen with an emission wavelength of $545\,nm$.

As the plates and phosphor must be independently biased with high voltage, a high degree of vacuum is maintained in this region and includes a pressure-gauge sensitive interlock that shuts down the MCP assembly power supplies to prevent damage in the event of a pressure spike. The MCP assembly is mounted in front of a mirror angled at 45° making the phosphor visible from a glass side port of the six-way cross. This port is enclosed by a shrouded blackout-box that contains a 1.3 megapixel digital CCD camera. This camera can be fan or water-cooled and can be operated manually or triggered via the sequencer with a set exposure time.

Mounted onto and directly beneath the MCP assembly housing is also an accelerator tube currently utilised in Ps yield studies to increase positron implantation depth.

3.4 Control System & Sequencer

3.4.1 Control Hardware

Like all modern experimental settings, a high degree of computer control and hardware monitoring is utilised by the user to design and execute experimental sequences and also allows the use of interlocks that maintain experimental conditions, prevent health and safety hazards, and mitigate damage to expensive equipment. While the pressures across the system are monitored by the appropriate vacuum gauges (see section 3.2.1), these values are read and recorded by controllers that allow for each gauge to be controlled manually and also via a LabVIEW virtual instrument which enables the user to constantly monitor each gauge and also allows interlock thresholds to be set that may for example, turn off the MCP, open or close a valve, or deactivate a sensitive cold cathode gauge. A similar arrangement is given to the 2nd and 3rd stage solenoid power supplies; the applied current is set and the current and voltages are monitored via PC. These power supplies have built-in over-voltage protection and a cut-off voltage can be set for scenarios where the closed-cycle water chiller fails and the magnet overheats. The 2nd stage electrodes are independently biased and electrically accessible through vacuum feedthroughs. The 1st stage electrodes (except the first 'gate' electrode) are connected via a series resistor chain housed in an external "bias box"; a total of eight electrical connections are made which can be viewed in figure 3.5, each of which are wired to the output of custom-made 'Llachar' amplifiers with a gain factor of 14. These receive and amplify $\pm 10\,\text{V}$ signals from the analog output (AO) channels of a NI PCI-6713 expansion card which is accessible via a NI-BNC2120 shielded connector block. The required potentials for each electrode are set by the user via LabVIEW software which configures a 1 million gate NI PCI-7811R field-programmable gate array (FPGA) that can trigger the AO device with a minimum state duration of $37.5\,\text{ns}$ and timing resolution of $12.5\,\text{ns}$ that also supplies digital TTL triggers to other hardware when required for a given sequence e.g., application of the rotating wall, triggering the camera, the digitiser etc.

3.4.2   Software Control & Implementation

Central to the apparatus is the software that drives it. Control is given to the user by two networked computers with one dedicated to designing and executing sequences. This sequencer computer primarily makes use of three custom-made LabVIEW virtual instruments (VIs): the Editor VI for designing individual sequences, the Modder VI for generating lists of randomly executed sequences to vary multiple parameters, and the Sequencer VI, the latter executes the loaded sequence and records the relevant information for data acquisition in the form of `.CH#` and `.CAM` files.

Whilst the modder VI is useful for efficiently acquiring very large multivariate data sets in an automated fashion over an extended time period, the experimental work presented here required careful observation of positron cloud conditions in order to determine that sequences were being correctly executed, the data properly recorded, and that experimental conditions were being maintained i.e., solenoids operational at set current, positrons clouds not impeded or blocked along the beamline etc. and therefore, the experiment primarily makes use of the editor VI to manually execute individual sequences whereby MCP images and positron annihilation signals can be readily observed. This is also necessary for acquiring an empirical parameter that may be required for further acquisition of data, such as the applied rotating wall frequency for which the smallest cloud (greatest axialisation) is achieved.

More detailed information on this system can be read in [43], the postgraduate thesis of C. A. Isaac, the program's developer. When creating a typical sequence using the LabVIEW interface, the duration (minimum of 37.5 ns) must be specified, and the appropriate digital channels activated to trigger any equipment that may be required along with the potential profile for the electrodes. A textbox to add a line descriptor allows for easy understanding and edits.

This extensive functionality allows for the creation of sequences for this work that apply the rotating wall with a linearly swept frequency by specifying and varying sequence parameters for f_S, f_E, τ_s and V_d; start frequency, end frequency, sweep time, and rotating wall amplitude, respectively.

Chapter 4

Chirp-Enhanced Axialisation

4.1 Experimental Method

This project seeks to investigate chirp-enhanced axialisation under a selection of three cooling gases with varying parameters. To accomplish this, positrons are initially accumulated in the trap during application of a static rotating wall field in the presence of a buffer gas (N_2) and cooling gas. This field will have a drive frequency that is resonant off-axis, increasing the lifetime of positrons in the trap but with less particle heating than the on-axis drive frequency, i.e., at $r = 0$. The frequency at which the axialisation rate, Γ (from equation 2.29) is highest in the trap is approximately $9.5\,\text{MHz}$ (for various SF_6 pressures) [42] as shown in figure 4.1 for three rotating wall amplitudes. After accumulation is stopped, the cloud is held in the well whilst the drive frequency is linearly swept to some end frequency in a chosen period, or sweep duration, τ_s. The cloud is subsequently ejected and detected by the MCP assembly and CsI(Tl) scintillator upon collective annihilation for all data presented, the buffer gas was administered at approximately $288\,\text{mbar}$ throughout the entire study.

The role of sweeping the rotating wall frequency to enhance positron cloud density can be seen in figure 4.4 where it is compared directly with the static, unchirped case. For each cooling gas used, the amplitude of the rotating wall and cooling gas pressure were varied.
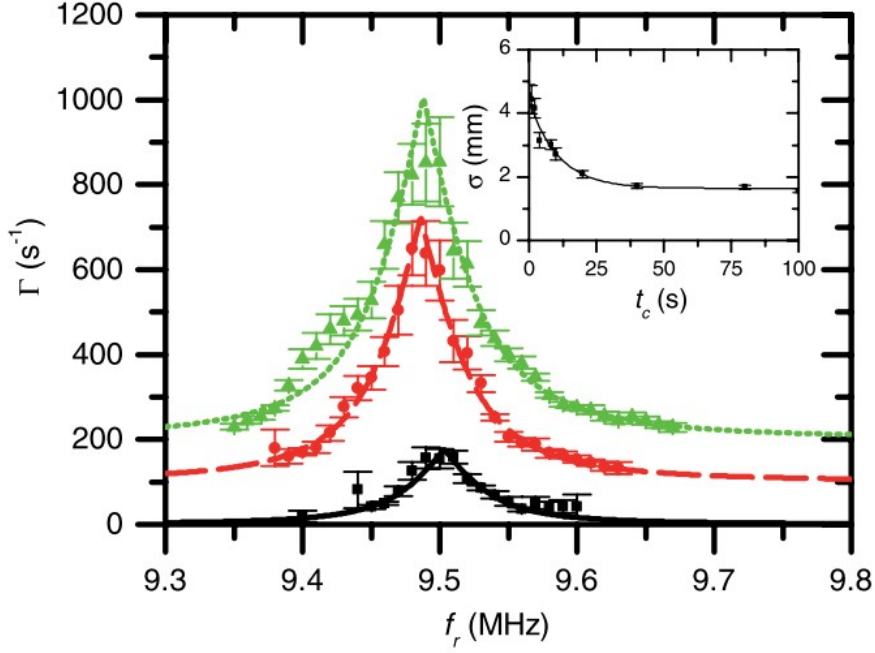
Figure 4.1: Compression rate, Γ as a function of applied rotating wall drive frequency, f_{RW} for three amplitudes: $75\,\text{mV}$ (■), $150\,\text{mV}$ (●), $225\,\text{mV}$ (▲), with the latter two offset by $100\,\text{s}^{-1}$ & $200\,\text{s}^{-1}$, respectively. Inset: An example of compression curve fit used to extract Γ. From [42].

4.1.1 Data Processing

The `.CAM` files recorded by the digital camera at the MCP are opened in *Wolfram Mathematica* and in a manner that maps each pixel value to its corresponding (x, y) coordinate. The intensity value data for each pixel is then fitted to a 2D Gaussian function of the form,

$$f(x, y) = A \exp\left[-\left(\frac{(x - x_0)^2}{2\sigma_x^2} + \frac{(y - y_0)^2}{2\sigma_y^2}\right)\right] + B \tag{4.1}$$

where $\sigma_x = \sigma_y$ is assumed. The extracted widths σ, are then plotted against the rotating wall end frequency, f_{E}. Before this can be done however, the region of interest must be isolated, namely, extraneous regions should be omitted so as not to skew the fit. This procedure is particularly important in this study due to a damaged or 'dead' region on the MCP. An example of an MCP image processed and analysed is shown in figures 4.2 and 4.3. These images show digital images of the MCP phosphor complete with 1D Gaussian 'slices' extracted from the centre. A 1D version of equation 4.1 is fitted to them. From the plots, it's evident that removing the compromised regions has a minimal effect in this case; it's possible

that the actual intensity per pixel could be lower than that extracted. A pair of 1D slices is also shown in figure 4.4; a comparison of before and after a chirp is applied. These data were also acquired using CsI detectors.
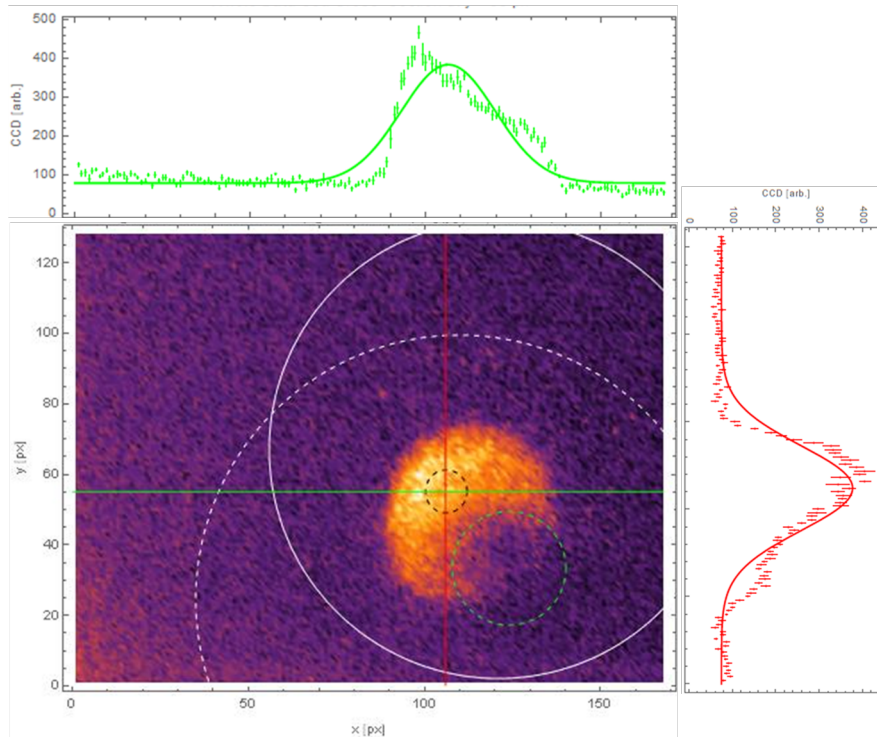
Figure 4.2: An MCP image. The green and red plots represent 1D slices fitted with Gaussian functions. The white dashed and solid circles represent the positions of the phosphor and pumping restriction, respectively. The green and black dashed circles represent MCP damage and Gaussian σ, respectively.
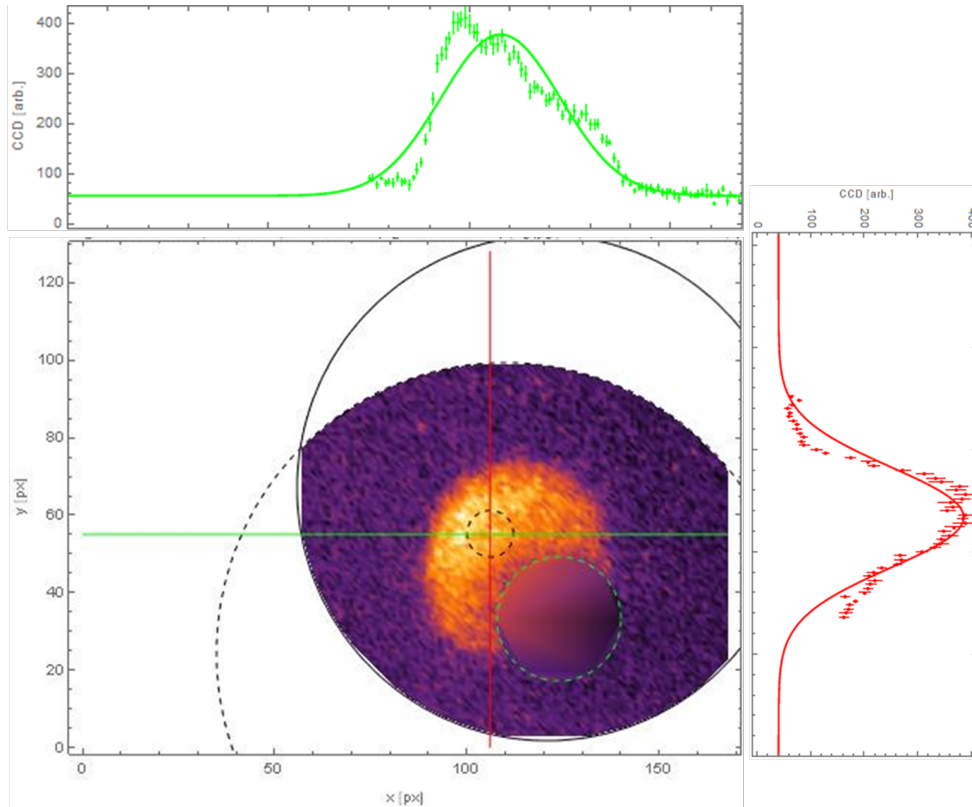
Figure 4.3: An MCP image after omission of extraneous data, the smooth damaged region is an artifact of Mathematica's image rendering procedure.
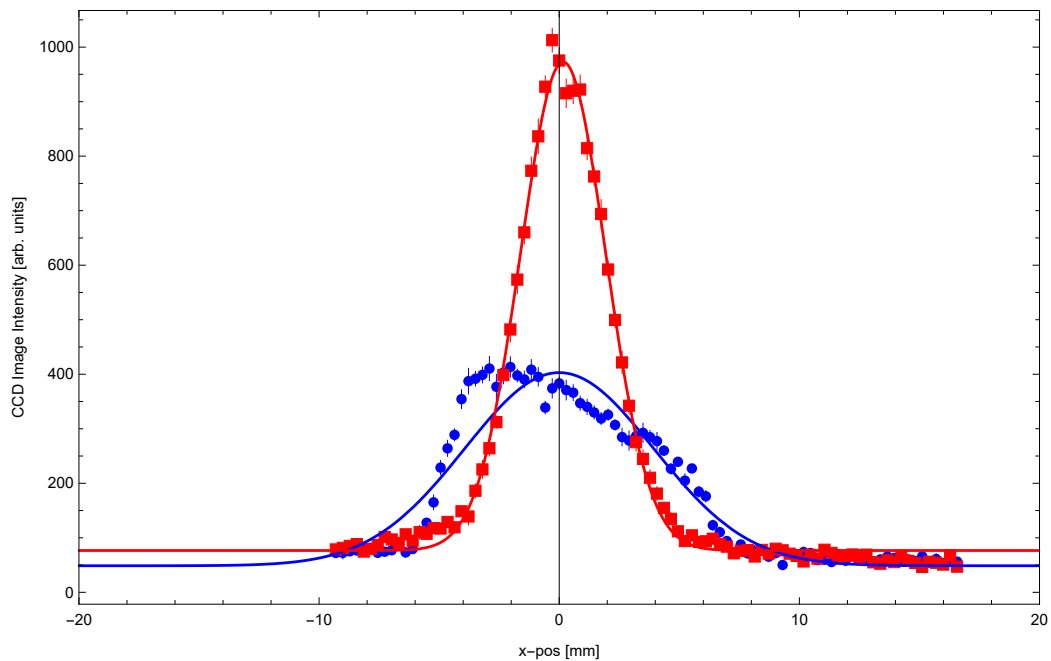
Figure 4.4: A 1D comparison of CCD Image Intensity for a cloud of positrons axialised with a rotating electric field at $9.45\,\mathrm{MHz}$ both before (●) and after (■) the rotating field is swept to $9.1\,\mathrm{MHz}$ in $100\,\mathrm{ms}$.

The `.CH0` and `.CH1` files that store the CsI detector data are more simply processed;

the signal heights are extracted from the traces by subtracting the peaks from the troughs.

4.2   Frequency Chirping

All data was recorded at cooling gas inlet pressures, recorded using capacitance gauges, of 0.665 mbar and 0.3325 mbar, for the gasses covered below.

4.2.1 SF_6

Sulphur hexafluoride is generally the most efficient cooling gas used when compressing a positron cloud, whereas carbon dioxide is typically used when compressing electrons due to SF_6 having a high affinity for molecular electron capture [66]. The CsI signal, which represents the estimated positron number, and the CCD image data is then processed. figures 4.5 and 4.6 display an example of these data for multiple rotating wall amplitudes after initial compression at 9.45 MHz at inlet cooling gas pressures of 0.665 mbar and 0.3325 mbar, respectively.

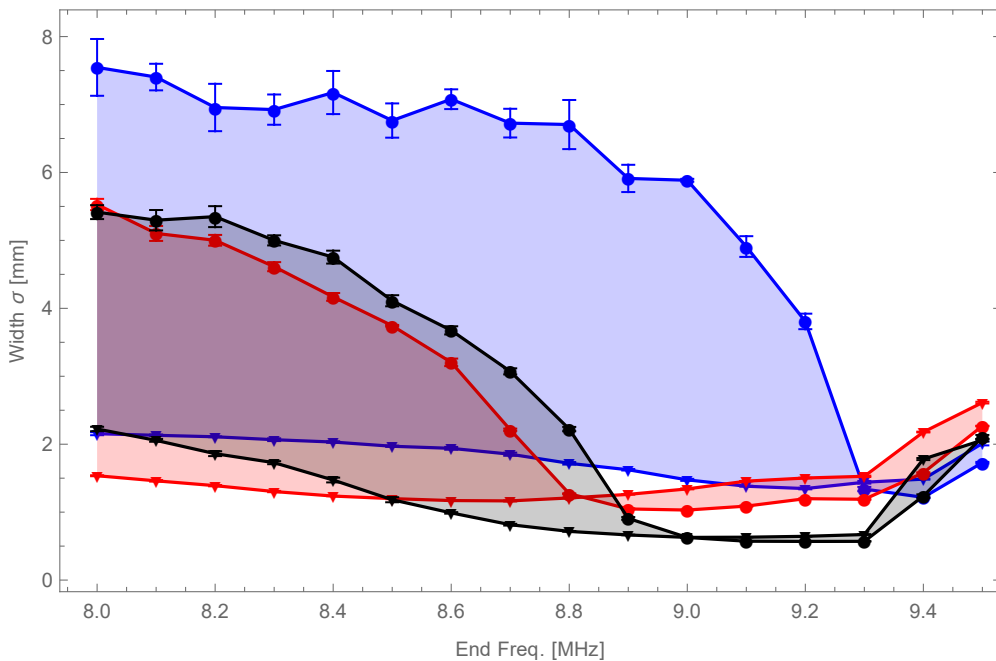**Figure 4.5:** Extracted widths σ at varying end frequencies for sweep durations between 25 ms (▼) and 300 ms (●). Data is visible for rotating wall amplitudes of 0.5 V (**blue**), 1 V (**red**), & 2 V (**black**). SF_6 was administered into X2 at 0.3325 mbar.
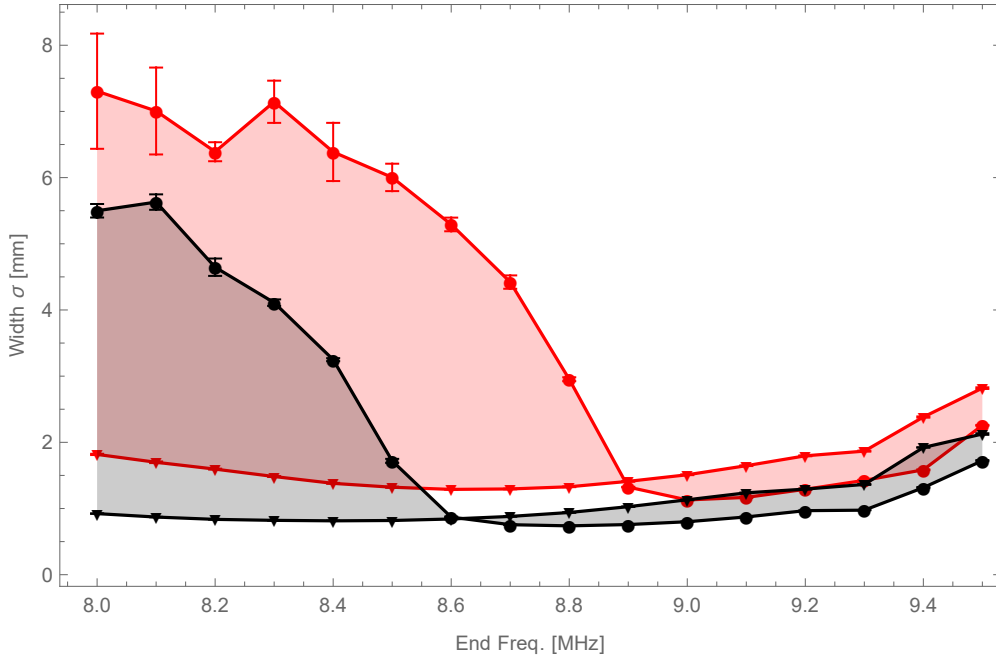
Figure 4.6: Extracted widths σ at varying end frequencies for sweep durations between 25 ms (▼) and 300 ms (●). Data is visible for rotating wall amplitudes of 1 V (**red**), & 2 V (**black**). SF_6 was administered into X2 at 0.665 mbar.

In an attempt to visualise the action of the frequency sweep in time, the accumulated cloud was ejected after increasing fractions of the sweep duration, for each duration. The results are visualised in figures 4.7 and 4.8. The latter figure has fits applied of the form in equation 2.33; whilst not the appropriate fit to use due to the compression rate's time dependence in the frequency-chirped case, it is worth noting the fits' approximate consistency with the data. In the form a density plot, the data acquired for SF_6 shown in figure 4.9 can be qualitatively compared with the data from [23], as shown in figures 2.10.

4.2.2 CF_4

Carbon tetrafluoride is also used as a cooling gas to mitigate rotating wall-induced heating, and has also seen some use as a buffer gas in lieu of molecular nitrogen, albeit an order of magnitude less efficient [60].

In this study, CF_4 was the cooling gas most often used and on which the sweep functionality was tested. Figure 4.10 displays widths at various end frequencies under different experimental conditions with the corresponding CsI signal traces shown in figure 4.11.
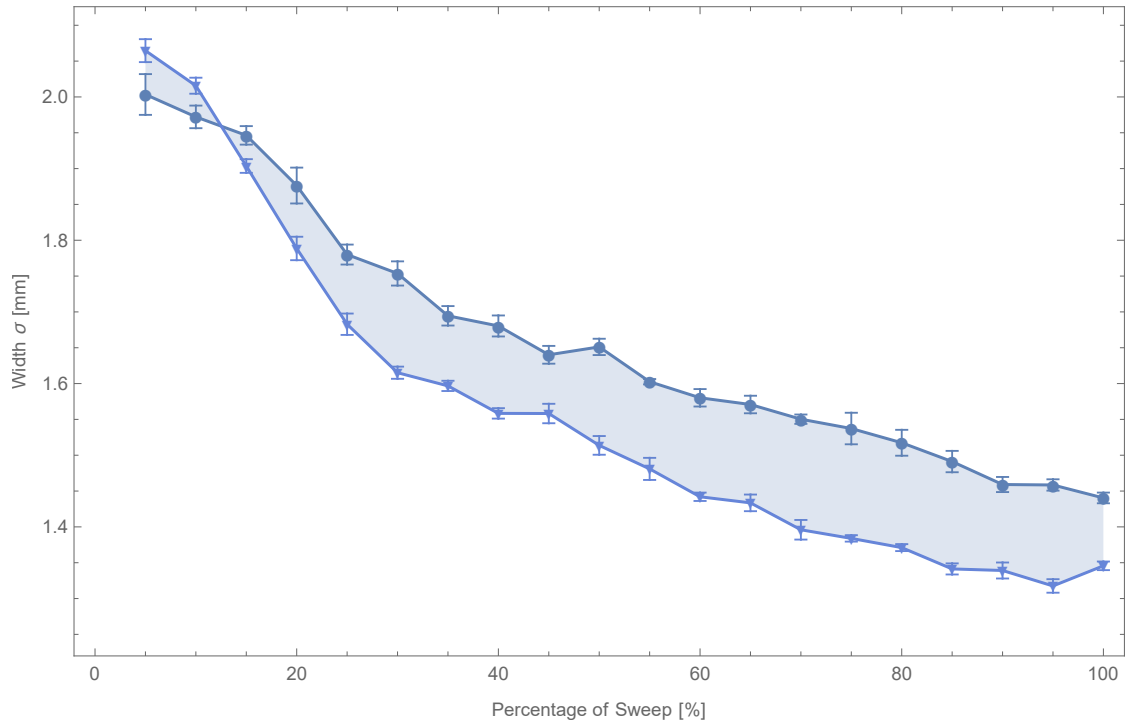
Figure 4.7: Extracted positron cloud widths as a function of sweep duration fraction completed prior to ejection (full data in fig. 4.8). The data shown is for sweep duration of 25 - 300 ms represented by (●) and (▼). respectively. SF_6 was administered at 0.665 mbar.
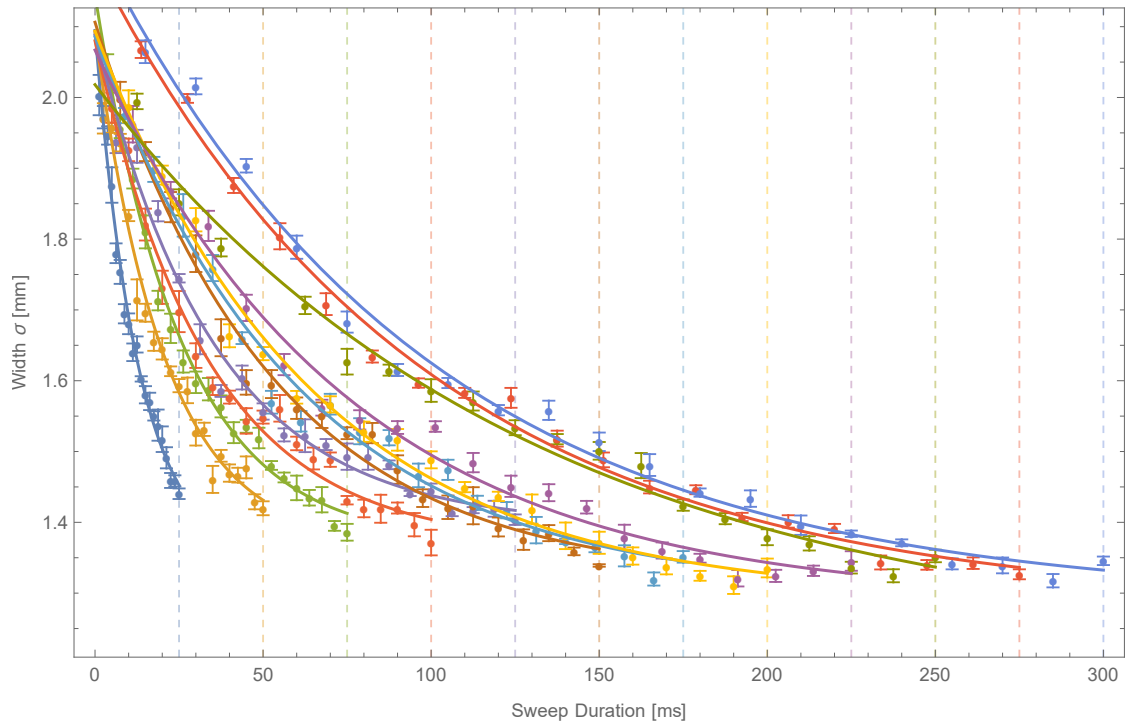
Figure 4.8: Extracted positron cloud widths as a function of their sweep duration. Each duration is marked at its end by a colour-matched y-axis gridline. The data are fitted with equation 2.33. SF_6 was administered at 0.665 mbar.
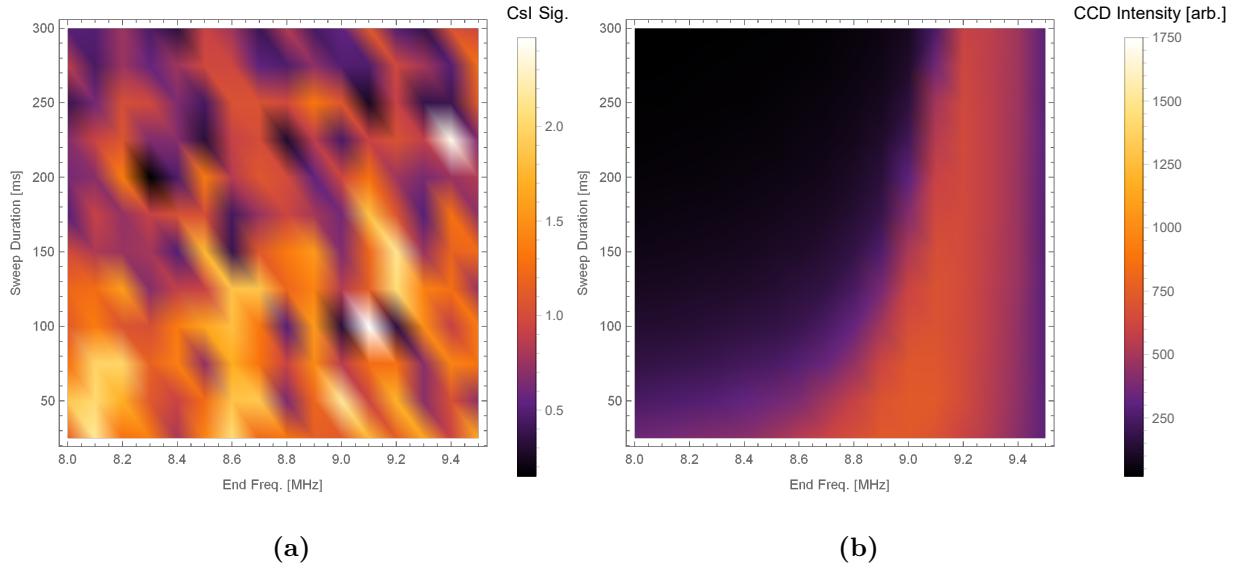
Figure 4.9: Density plots of CsI signal (**a**) and CCD image intensity (**b**) of ejected positrons clouds having undergone rotating wall frequency sweeps to varying end frequencies in varying sweep durations after an initial compression at $500\,mV$ & $9.5\,MHz$. The SF_6 was administered at an inlet pressure of $0.3325\,mbar$.
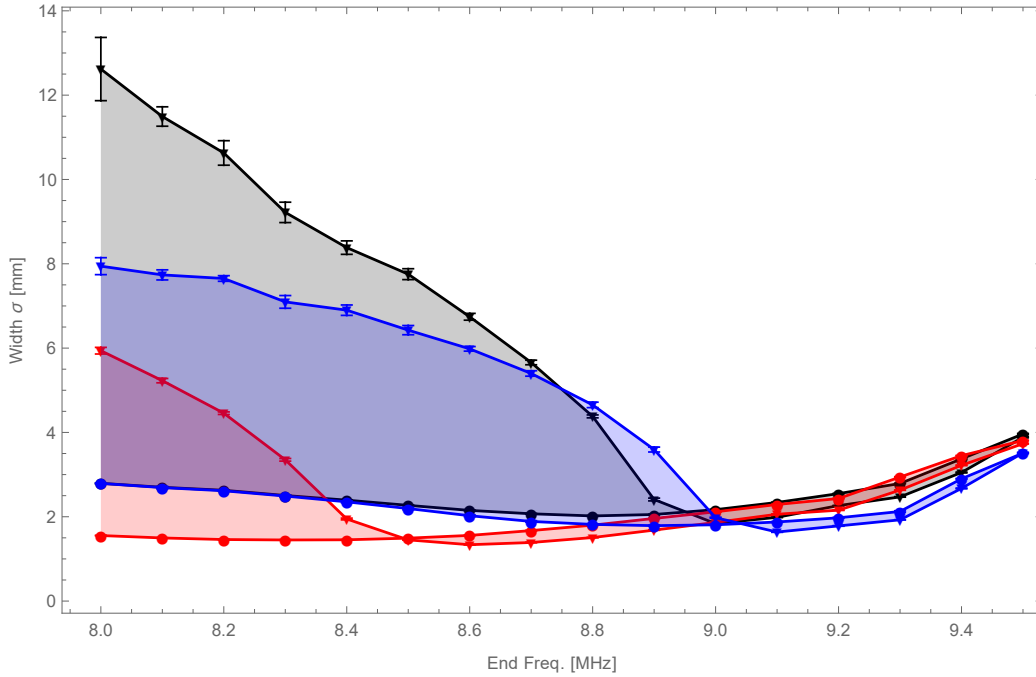
Figure 4.10: Extracted widths σ, at varying end frequencies. Each data set shows the span from $\tau_S = 25$ - $300\,ms$ (● - ▼). Each data set has the parameters: **Black** → RWA $= 0.5\,V$, PG11 $= 0.665\,mbar$, blue → RWA $= 0.5\,V$, PG11 $= 0.3325\,mbar$, red → RWA $= 1\,V$, PG11 $= 0.665\,mbar$.
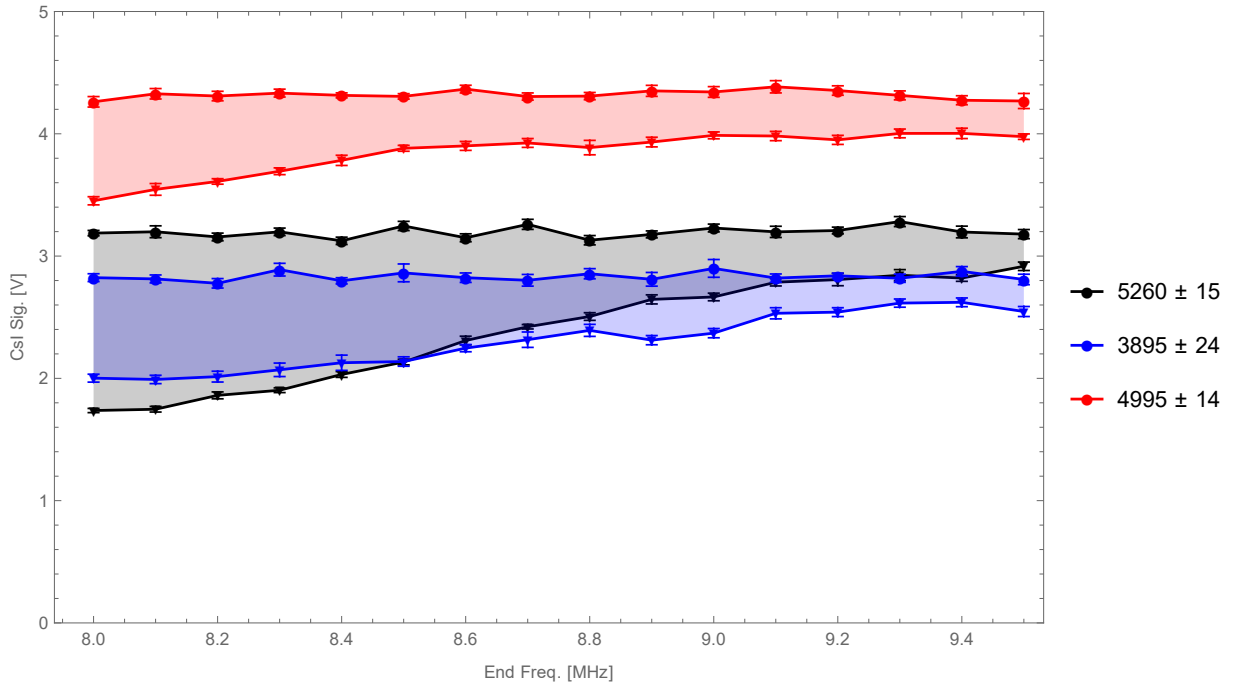
Figure 4.11: Recorded CsI signals corresponding to fig. 4.10. The legend numbers represent the approximate count rate of positrons entering the accumulator the day each data set was recorded.

Of immediate note is that a lower width is achieved for all frequencies when less cooling gas is used with a lower rotating wall amplitude. Despite this, a smaller minimum width (and a higher peak central density) is achieved with a stronger drive of $1\,\text{V}$ when used with a sufficient quantity of cooling gas. It should also be noted that whilst a higher quantity of cooling gas facilitated a greater degree of initial axialisation, the $1\,\text{V}$ case may also be partially effected by detector saturation. An overall example of the peak central density for the two gas pressures, represented by the extracted peak CCD image intensity is shown in figure 4.12.

(a)

(b)
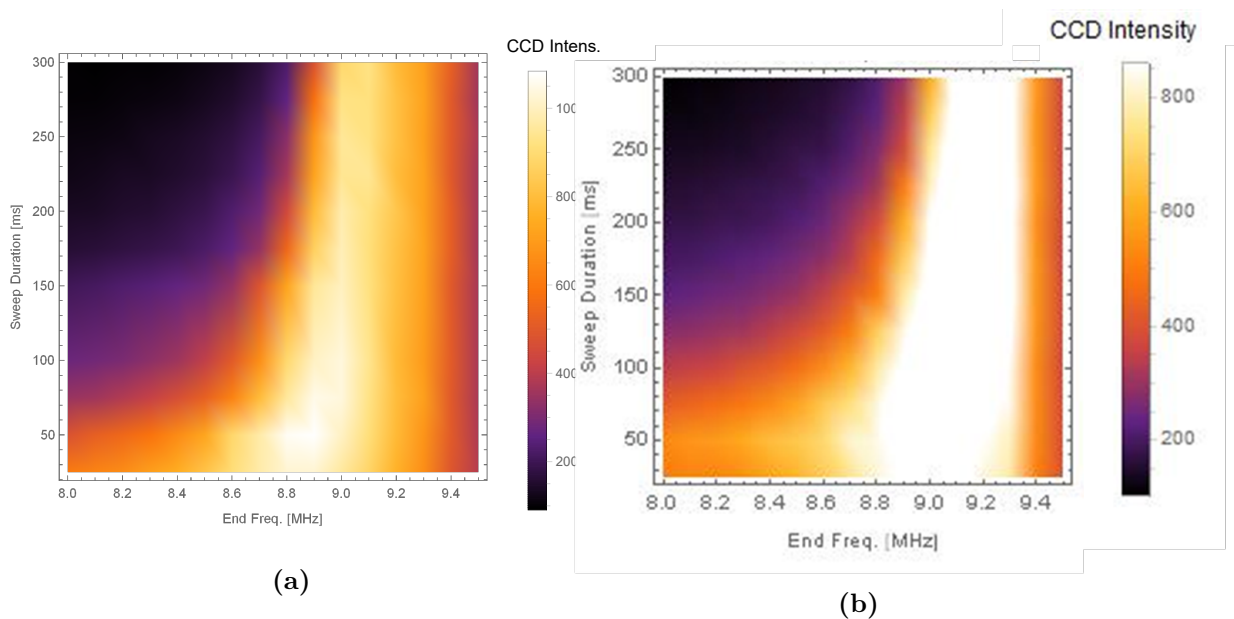
Figure 4.12: Density plots of CCD image intensity for CF_4 gas with RWA $= 0.5$ V. (**a**) represents the data when CF_4 inlet pressure was 0.3325 mbar and (**b**) represents the data at 0.665 mbar.

4.2.3   CO

A small amount of data was acquired with carbon monoxide as the cooling gas to investigate the chirp effect on a less typically used species. As per table 2.1, CO has a longer cooling time than both SF_6 and CF_4 and is generally recognised as a relatively inefficient cooling gas. As such, the clouds produced were typically more diffuse. Density plots highlighting the central density and CsI signal data that was acquired with this gas are shown in figures 4.13 and 4.14.
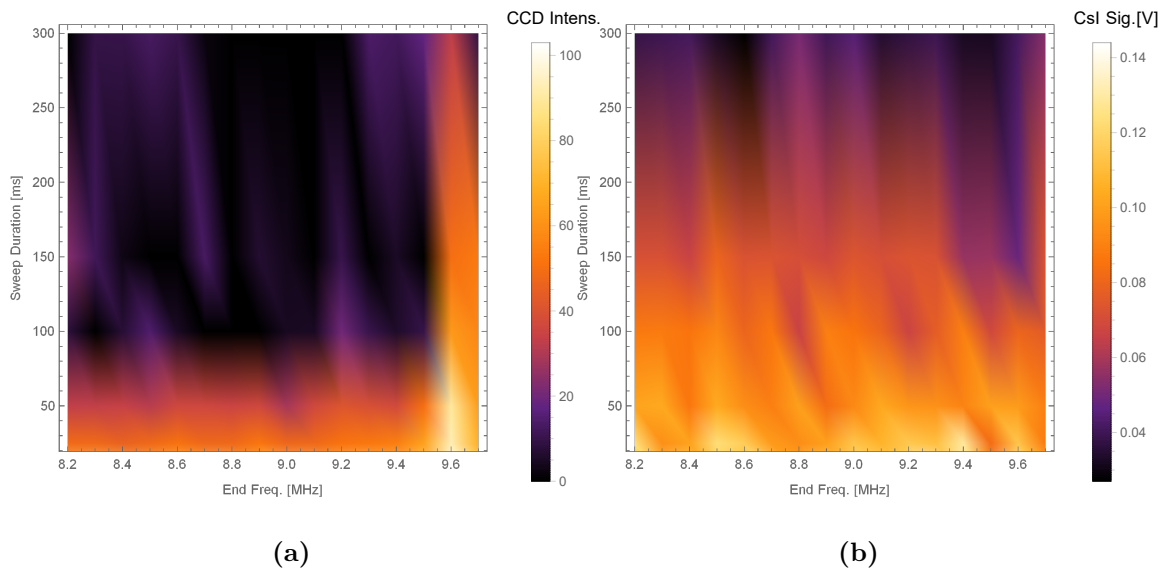
Figure 4.13: Density plots for (**a**) CCD image intensity and (**b**) CsI signal for a range of end frequencies and sweep duration. The cooling gas is CO at an administered pressure of 0.3325 mbar.
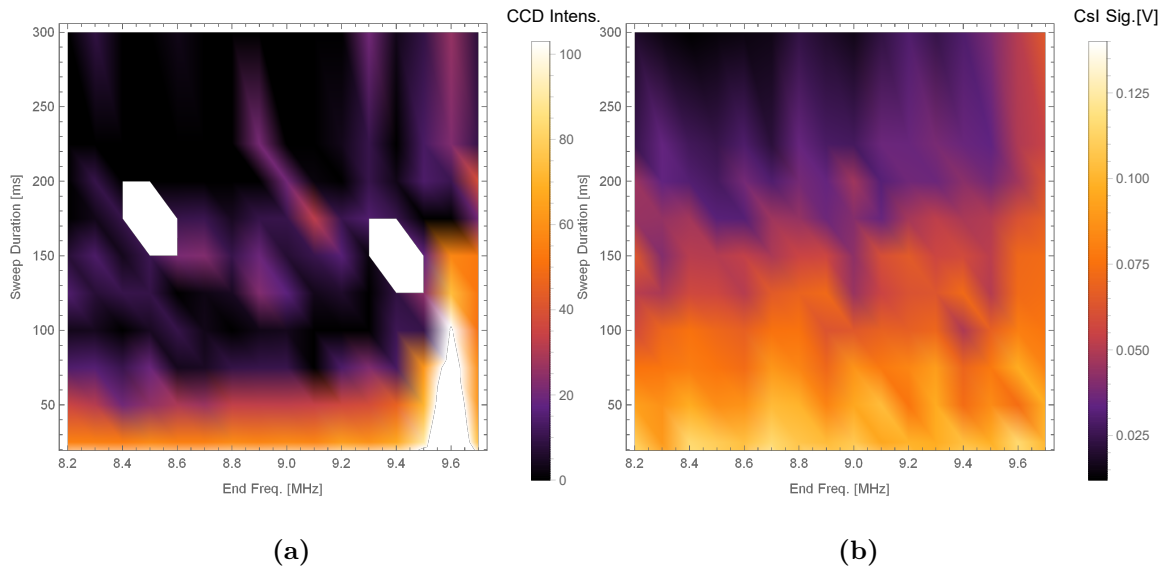
Figure 4.14: Density plots for (**a**) CCD image intensity and (**b**) CsI signal for a range of end frequencies and sweep duration. The cooling gas is CO at an administered pressure of 0.665 mbar. The two white regions are areas of anomalous saturation. The higher peak intensity (and small cloud width) is partially a result of positron loss, possibly due to increased CO pressure.

4.3 Numerical Model

4.3.1 Overview

An attempt was made to roughly compare the data with a simplistic toy model under several approximations. By modifying equation 2.32 such that the bounce frequency ω_z is dependent on the particles' radial distance from the trap centre and kinetic energy, and substituting in equation 2.29 for Γ, we arrive at a differential equation for an individual particle trajectory,

$$\dot{r}(t) = -\Gamma\left[r(t), t\right] r(t) + \gamma. \tag{4.2}$$

This equation cannot be solved to produce an analytical expression in the same way as equation 2.33. Instead it was evaluated numerically using *Wolfram* Mathematica's in-built `NDSolve[]` command. To quantify the axial bounce frequency in a simple way without being computationally intensive, ω_z was approximated using the equation,

$$\omega_z(r) \approx \omega_{z_0} + c_1 r^2 \tag{4.3}$$

where ω_{z_0} is the on-axis bounce frequency i.e., when $r = 0$, and c_1 is taken to be constant. Since the typical extent of the positron clouds used in this study are $\lesssim 10\,\text{mm}$, considering only the initial series of r values is a reasonable approximation. This can be observed in figure 4.15 which shows a comparison of the approximation with a more thorough and time-intensive calculation, utilising the equation,

$$\frac{1}{f_z(E, r)} = \sqrt{\frac{2m}{q}} \int_{z_1}^{z_2} \frac{\mathrm{d}z}{\sqrt{E - \phi(E, r)}}. \tag{4.4}$$

More detail on how the full calculation was involved, including mapping of the solution to the Laplace equation (equation 2.20), can be found in [23].

The differential equation was evaluated first for a single particle case and then a group case, the latter intended to model an aggregate of particles or, a positron cloud, though it does not consider particle self-interactions. A half normal distribution of r_0 values was generated (and multiplied randomly with ± 1 to produce a normal distribution) with its mean and standard deviation informed by parameters
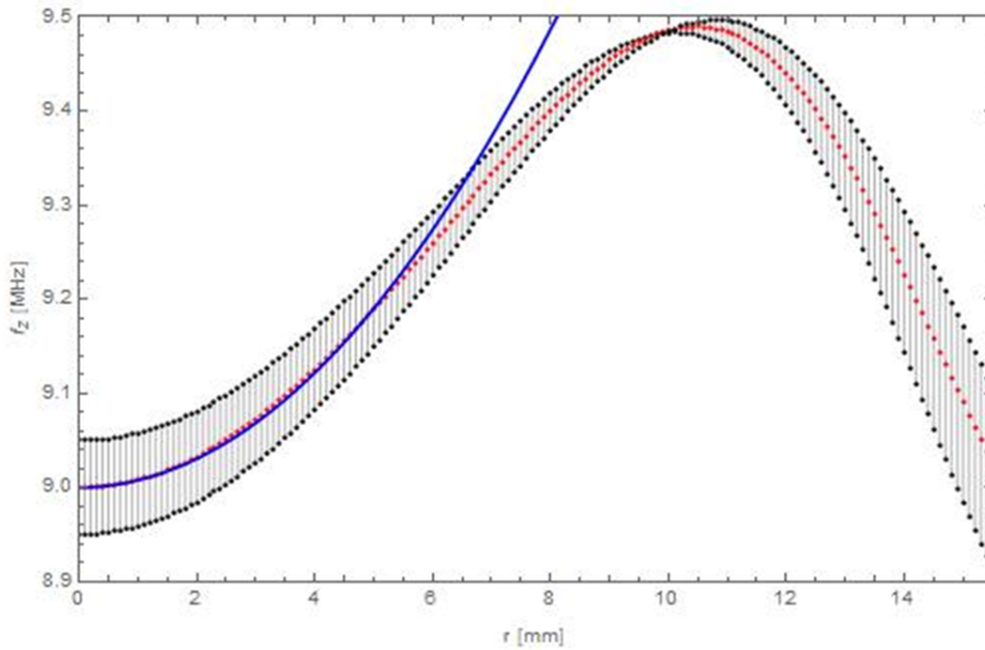
Figure 4.15: A comparison of the axial bounce frequency calculation as a function of radial position relative to the trap centre (red with **black** error bars), and the approximation of equation 4.3 (blue). Here, $\omega_{z_0} = 9\,\mathrm{MHz}$.

extracted from the fit of the static rotating wall case i.e., the cloud as it would be just before the chirp is applied. The group model was mapped over the distribution to generate an array of numerical solutions for $r(t)$. The 'width' of the distribution at the end of the sweep is then extracted, as can be visualised in figure 4.16.
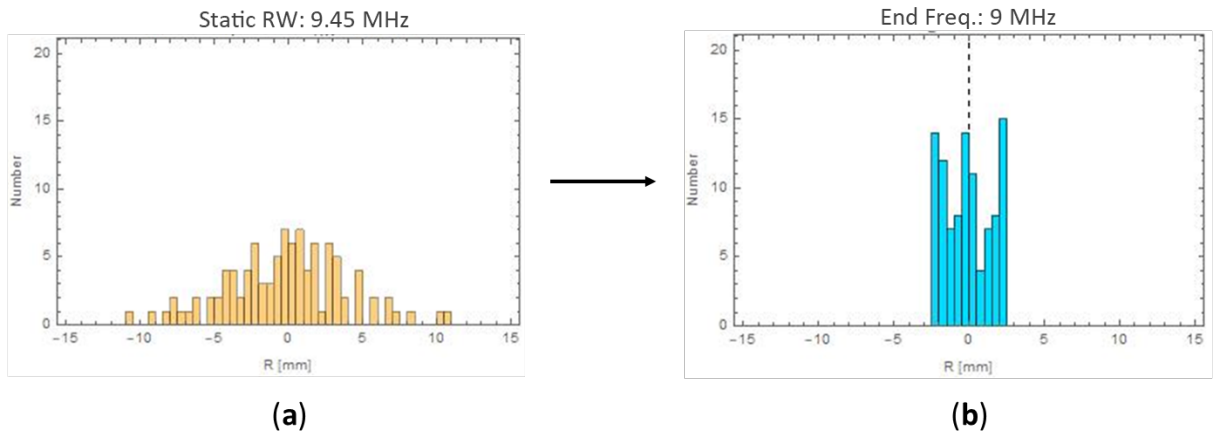
Figure 4.16: Qualitative comparison of modelled 'cloud widths' in the form of histograms. (**a**): After the static rotating wall is applied with at $9.45\,\mathrm{MHz}$ i.e., $r(t = 0)$. (**b**): The distribution after chirp is applied to an end frequency of $9\,\mathrm{MHz}$.

The plots above show theoretically that applying a sweep/chirp after an initial static compression, results in further increase in density of the positron cloud.

4.3.2 Comparison with Data

As the model is relatively simplistic and makes several approximations, only a qualitative comparison with data is presented here. The density plots can be observed in figure 4.17.
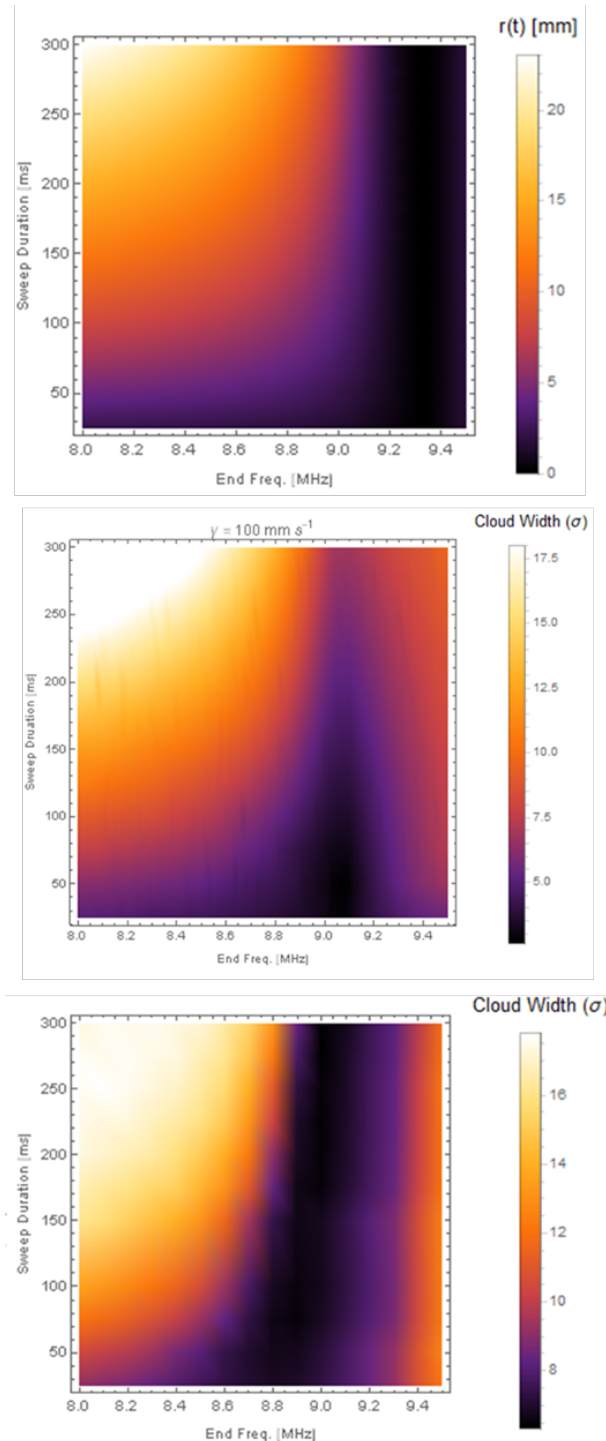
Figure 4.17: Top: The single particle case. **Middle**: The group model case. **Bottom**: Experimental data acquired using CF_4 as the cooling gas.

From the images above, a visual comparison between the simplistically modelled data and the experimental data could be considered consistent. A more thorough and extensive analysis should be pursued for a better interpretation of the results. However, a brief outlook is presented overleaf.

Chapter 5

Conclusions & Future Work

5.1 Data - Interpretations

Of the three cooling gases tested, each exhibited, at least on a qualitative level, an ability to mitigate induced heating relative to each other that is commensurate with the expected capability of the gas when the static rotating wall is applied. Namely, SF_6 generally led to lower positron losses than for CF_4 and CO. Whilst CF_4 underwent the most testing, it was always necessary to apply the chirp to the positron cloud whilst using SF_6 to compare somewhat directly with the previous data obtained by [23]. CO was tested under the initial assumption that due to its longer cooling time, it would be a less efficient option regardless of static or chirped rotating wall application. In agreement with the study conducted by Deller *et al.*, positron densities were improved at lower drive amplitudes and cooling gas pressures with the chirp applied, though the highest densities were still achieved with higher amplitudes if the cooling gas pressure were sufficiently high. This appears the same across the gases tested.

The smallest widths were consistently found at τ_s meaning therefore, that no benefit arises from ejecting the positron cloud early. This 'chirp-in-action' can be visualised in figure 4.7. Incidentally, curves of this nature could, within a degree of uncertainty and dependent on the number of positrons accumulated, be used to effectively select a positron cloud width.

5.2   Outlook

As mentioned in section 2.3.2, we can infer from equation 2.29 that maximum compression Γ_{max}, is achieved when $\omega_{\mathrm{RW}} = \omega_0$, in particular,

$$\Gamma_{\mathrm{max}} = \frac{\kappa}{4}. \tag{5.1}$$

Whilst this equation neglects any upper limit for the compression rate as a function of any damping κ, the maximum compression condition makes more physical sense. This project sought to further investigate the effect of sweeping or "chirping" the rotating wall frequency downward with the hope of following the changing r-dependent centre frequency ω_0, thus better maintaining the maximum compression condition i.e., $\omega_{\mathrm{RW}}(t) = \omega_0(r)$. The results of this preliminary study suggest how sweeping the rotating wall frequency, making it dynamic instead of static could, in the first instance be a method of acquiring denser, smaller clouds at lower cooling gas pressures and drive amplitudes thus making the process more efficient. It also leads to insight into the limits of rotating wall compression of positron clouds in the single-particle regime (i.e., non-plasma). In particular, if the maximum compression condition was maintained perfectly (ideal case), what would then be the main limitation of cloud density/width, beyond particle self-interaction?

Future work would be best focused on producing and refining a more complex and extensive numerical model, potentially utilising a virtual ion trajectory simulation environment such as SimIon® or COMSOL®. A more developed treatment of the damping parameter to more accurately simulate the effects of background gases would further enhance an investigative model instead of the simplistic and highly approximate Stokes viscous drag term employed here.

From an experimental perspective, it is clear from this work that the optimum cooling gas to use when performing chirp studies of the rotating wall is congruent to that used for the static case i.e., SF_6.

All of the data acquired in this study concerned positron clouds receiving a drive amplitude that was the same in the static compression phase and throughout the chirp. Introducing separate drive amplitudes for the separate phases of the sequence may allow for exploration of the effects of the chirp on particle heating and width

limits. Finally, this study made use of a 'standard' linear frequency sweep function as shown in equation 2.35; it may be conducive to investigate other functional forms for $\omega_{\mathrm{RW}}(t)$, such as an exponential sweep,

$$\omega_{\mathrm{RW}} \to \omega_{\mathrm{RW}}(t) = \omega_0 \left(\frac{\omega_{\mathrm{E}}}{\omega_{\mathrm{S}}} \right)^{\frac{t}{\tau_{\mathrm{S}}}} \tag{5.2}$$

also known as a geometric sweep.

Ideally, the rate at which the centre frequency ω_0 changed would undergo some form of digital frequency modulation or some other form of encoding which could then be matched with a corresponding drive frequency ω_{RW} in real-time.

Ultimately, chirp-enhanced compression, whilst not the optimal approach for attaining maximum positron densities (or minimum widths), would indeed serve as a novel way of increasing the efficacy of any cooling gas when applying the rotating wall at lower amplitudes and is worth further investigation to fully explore the intricacies of the rotating wall method.

Bibliography

1. Schuster, A. Potential Matter - A Holiday Dream. *Nature* **58,** 367 (1898).

2. Dirac, P. The Quantum Theory of the Electron. *Proceedings of the Royal Society A.* **117,** 610–624 (1928).

3. Dirac, P. Quantised Singularities in the Quantum Field. *Proceedings of the Royal Society A.* **133,** 60–72 (1931).

4. Anderson, C. The Positive Electron. *Physical Review* **43,** 491–494 (1933).

5. *Atop the Physics Wave: Rutherford Back in Cambridge, 1919-1937* %7Bhttps: //history.aip.org/history/exhibits/rutherford/sections/atop- physics-wave.html%7D.

6. Charlton, M. *et al.* Positron production using a 9 MeV electron linac for the GBAR experiment. *Nuclear Instruments and Methods in Physics Research A* **985,** 33 (2021).

7. Howell, R. *et al.* Production and use of low-energy, monoenergetic positron beams from electron LINACS. *Applied Physics A* **43,** 247–255 (1987).

8. Joliot, M. & Curie, I. Un Nouveau type de radioactivité. (French) [A new type of radioactivity]. *J. Phys* **5,** 254 (1934).

9. Charlton, M. & Humbertson, J. *Positron Physics* (Cambridge University Press, 2000).

10. Cherry, W. *Secondary Electron Emission Produced from Surface by Positron Bombardment* PhD thesis (1958).

11. Brown, B. A cobalt 58 'slow positron generator'. *Applied Surface Science* **116,** 204–107 (1997).

12. Galan, M. *Table de Radionucléides* `http://www.nucleide.org`. (accessed: 29.10.2021).

13. Knoll, G. *Radiation Detection & Measurement* 4th (Wiley, 2010).

14. Coleman, P. *Positron Beams and their Applications* (World Scientific, 2000).

15. Kerrigan, S. *An Experimental Study of Positron Moderation and Accumulation and the Laser Ionisation of Positronium* PhD thesis (2011).

16. Madey, J. Evidence for the emission of slow positrons from polyethylene. *Phys. Rev. Lett.* **22,** 784–786 (1969).

17. Canter, K. *et al.* Measurement of total cross sections for low energy positron-helium collisions. *J. Phys. B: Atom. Molec. Phys.* **5,** 7 (1972).

18. Mills Jr., A. Efficient generation of low-energy positrons. *Appl. Phys. Lett.* **35,** 427–429 (1979).

19. Vehanen, A. *et al.* Improved slow-positron yield using a single crystal tungsten moderator. *Appl. Phys. A* **32,** 163–167 (1983).

20. Mills Jr., A. & Gullikson, E. Solid neon moderator for producing slow positrons. *App. Phys. Lett.* **49,** 1121–1123 (1986).

21. Bertsche, W. A., Charlton, M. & Eriksson, S. Cold neutral atoms via charge exchange from excited state positronium: A proposal. *New Journal of Physics* **19.** ISSN: 13672630 (2017).

22. Caravita, R. *et al. Positronium Rydberg excitation diagnostic in a 1T cryogenic environment* in. **2182** (2019), 030002.

23. Deller, A. *Positron Accumulation and Laser Excitation of the Positronium Atom* PhD thesis (2013).

24. Mortensen, T. *Manipulation of the magnetron orbits of particles and clouds in a two-stage buffer gas accumulator* PhD thesis (2013).

25. Deller, A. *et al.* Radially selective inward transport of positrons in a Penning-Malmberg trap. *New Journal of Physics* **16,** 073028 (2014).

26. *Nobel Prize in Physics 1989* (1989). `https://www.nobelprize.org`. (accessed: 10.03.2022).

27. Earnshaw, S. On the nature of the molecular forces which regulate the constitution of the luminiferous ether. *Trans. Camb. Philos. Soc.* **7,** 97–112 (1842).

28. Paul, W. Electromagnetic traps for charged and neutral particles. *Reviews of Modern Physics* **62,** 531–540 (1990).

29. Blaum, K., Novikov, Y. N. & Werth, G. Penning Traps as a Versatile Tool for Precise Experiments in Fundamental Physics. *Contemporary Physics* **51,** 149–175 (2010).

30. Major, F., Gheorghe, V. & Werth, G. *Charged Particle Traps. Physics and Techniques of Charged Particle Confinement* (Springer, 2005).

31. Estrada, J. *Cold Trapped Positrons and Progress to Cold Antihydrogen* PhD thesis (2002).

32. Surko, C., Leventhal, M., Crane, W. & Mills Jr., A. The Positron Trap - A New Tool for Plasma Physics, 221–233 (1984).

33. *NIST Chemistry WebBook: N_2* NIST, 2021. `https://webbook.nist.gov/cgi/cbook.cgi?ID=C7727379&Mask=1000`.

34. Marjanović, S. & Petrović, Z. Monte Carlo modeling and optimization of buffer gas positron traps. *Plasma Sources Science and Technology* **26,** 024003 (2017).

35. Huang, X., Anderegg, F., Hollmann, E., *et al.* Steady-State confinement of non-neutral plasmas by rotating electric fields. *Physical Review Letters* **78,** 875–879 (1997).

36. Heinzen, D. *et al.* Rotational equilibria and low-order modes of a non-neutral ion plasma. *Physical Review Letters* **66,** 2080–2083 (1991).

37. Wineland, D. & Dehmelt, H. Line shifts and widths of axial, cyclotron and G-2 resonances in tailored, stored electron (ion) cloud. *International Journal of Mass Spectrometry and Ion Physics* **16,** 338–342 (1975).

38. Greaves, R. & Surko, C. Radial compression and inward transport of positron plasmas using a rotating electric field. *Physics of Plasmas* **8,** 1789–1885 (2001).

39. Anderegg, F., Hollmann, E. M. & Driscoll, C. F. Confinement of Pure Electron Plasmas Using Trivelpiece-Gould Modes. *Physics Review Letters,* 4875–4878 (1998).

40. Greaves, R. & Moxom, J. Compression of trapped positrons in a single particle regime by a rotating electric field. *Physics of Plasmas* **15,** 072304 (2008).

41. Isaac, C. A. Motional sideband excitation using rotating electric fields. *Physical Review A - Atomic, Molecular, and Optical Physics* **87,** 1–7 (2013).

42. Isaac, C. A., Baker, C. J., Mortensen, T., Van Der Werf, D. P. & Charlton, M. Compression of positron clouds in the independent particle regime. *Physical Review Letters* **107.** ISSN: 00319007 (July 2011).

43. Isaac, C. A. *Axialisation of Particles in a Penning-type Trap by the Application of a Rotating Dipole Electric Field and its Application to Positron Accumulation* PhD thesis (2010).

44. Marjanović, S., Banković, A., Cassidy, D., *et al.* A CF$_4$ based positron trap. *Journal of Physics B: Atomic, Molecular and Optical Physics* **49,** 215001 (2016).

45. Amoretti, M. *et al.* Production and Detection of Cold Antihydrogen Atoms. *Nature* **419,** 456–459 (2002).

46. *The Antiproton Decelerator* CERN. https://home.cern/science/accelerators/antiproton-decelerator. (accessed: 05.08.2022).

47. *The ALPHA Experiment* CERN. https://alpha.web.cern.ch/. (accessed: 05.08.2022).

48. Clarke, J., Van Der Werf, D., *et al.* Design and operation of a two-stage positron accumulator. **77,** 2–6 (2006).

49. Clarke, J., Van Der Werf, D., *et al.* Developments in the Trapping and Accumulation of Slow Positrons using the Buffer Gas Technique, 178–183 (2003).

50. Clarke, J. *The Generation and Manipulation of Low Energy Positron Beams* PhD thesis (2005).

51. Baker, C., Van Der Werf, D., Beddows, D., *et al.* Weakly bound positron-electron pairs in a strong magnetic field. *Journal of Physics B: Atomic, Molecular and Optical Physics* **41,** 4–10 (2008).

52. Hessels, E. A., Homan, D. M. & Cavagnero, M. J. Two-stage Rydberg Charge Exchange: An Efficient Method for Production of Antihydrogen. *Physics Review A* **57,** 1668 (1998).

53. Charlton, M. Antihydrogen Production in Collisions of Antiprotons with Excited States of Positronium. *Physics Letters A* **143,** 143–146 (1990).

54. Watkeys, P. *Towards Laser Excitation of Positronium and Advances in Positron Accumulation Techniques* PhD thesis (2008).

55. Deller, A. *et al.* Exciting positronium with a solid-state UV laser: The Doppler-broadened Lyman-α transition. *Journal of Physics B: Atomic, Molecular and Optical Physics* **48,** 175001 (2015).

56. Baker, C. *Studies of magnetized positronium and of positron dynamics in a rotating dipolar electric field* PhD thesis (2010).

57. Mortensen, T., Deller, A., Isaac, C. A., *et al.* Manipulation of the magnetron orbit of a positron cloud in a Penning trap. *Physics of Plasmas* **20,** 012124 (2013).

58. Fitzpatrick, R. *The Physics of Plasmas* 32–35. `https://farside.ph.utexas.edu/teaching/plasma/lectures1/index.html` (University of Texas).

59. Naidoo, C., van der Meulen, N. P., Vermeulen, C. & Krause-Rehberg, R. *The Production of ^{22}Na Positron Sources at iThemba LABS* in. 16th International Conference on Positron Annihilation (ICPA16) (Halle).

60. Baker, C., Isaac, C., Edwards, D., *et al.* Investigation of buffer gas trapping of positrons. *Journal of Physics B: Atomic, Molecular and Optical Physics* **53,** 185201 (2020).

61. Khatri, R., Charlton, M., *et al.* Improvement of rare-gas solid moderators by using conical geometry. *Applied Physics Letters* **57,** 2374–2376 (1990).

62. Edwards, D. *Efficient Excitation of Rydberg Positronium* PhD thesis (2019).

63. Deller, A. *Accumulator 3.1.pdf* Feb. 18, 2013. (accessed: 17.05.2022).

64. Saint-Gobain. *Scintillation Crystals* `https://www.crystals.saint-gobain.com`. (accessed: 16.02.22).

65. Clayton, R. *MCP and Accelerator 1.png* Nov. 21, 2018. (accessed: 12.05.2022).

66. Gerchikov, L. & Gribakin, G. Electron attachment to SF_6 and lifetimes of SF_6 negative ions. *Physical Review A* **77,** 042724 (2008).